Geological Magazine

www.cambridge.org/geo

Tectonic evolution of the South Altyn, NW China: constraints by geochemical, zircon U–Pb and Lu–Hf isotopic analysis of the Palaeozoic granitic plutons in the Mangya area

Nan Xu, Cai-lai Wu, Yuan-Hong Gao, Min Lei, Kun Zheng and Dong Gao

Key Laboratory of Deep-Earth Dynamics of MLR, Institute of Geology, Chinese Academy of Geological Sciences, Beijing 100037, China

Original Article

Cite this article: Xu N, Wu C, Gao Y-H, Lei M, Zheng K, and Gao D (2020) Tectonic evolution of the South Altyn, NW China: constraints by geochemical, zircon U–Pb and Lu–Hf isotopic analysis of the Palaeozoic granitic plutons in the Mangya area. *Geological Magazine* **157**: 1121–1143. https://doi.org/10.1017/S0016756820000126

Received: 31 May 2019
Revised: 31 January 2020
Accepted: 2 February 2020
First published online: 14 May 2020

Keywords:
South Altyn Orogenic Belt; Mangya; early Palaeozoic; zircon U–Pb and Lu–Hf isotopic data

Author for correspondence:
Cailai Wu, Email: wucailai@126.com

Abstract

The South Altyn Orogenic Belt (SAOB) is one of the most important orogenic belts in NW China, consisting of the South Altyn Continental Block and the Apa–Mangya Ophiolitic Mélange Belt. However, its Palaeozoic tectonic evolution is still controversial. Here, we present petrological, geochemical, zircon U–Pb and Lu–Hf isotopic data for the Mangya plutons with the aim of establishing the Palaeozoic tectonic evolution. We divide the Early Palaeozoic magmatism in the Apa–Mangya Ophiolitic Mélange Belt into four episodes and propose a plate tectonic model for the formation of these rocks. During 511–494 Ma, the South Altyn Ocean (SAO) was in a spreading stage, and some shoshonite series, I-type granitic rocks were generated. From 484 to 458 Ma, the oceanic crust of the SAO subducted northward, accompanied by large-scale magmatic events resulting in the generation of vast high-K calc-alkaline series, I-type granitic rocks. During 450–433 Ma, the SAO closed, and break-off of the subducted oceanic slab occurred, with the generation of some high-K calc-alkaline series, I–S transitional type granites. The SAOB was in post-orogenic extensional environment from 419 to 404 Ma, and many A-type granites were generated.

1. Introduction

The evolution of orogenic belts is generally accompanied by various magmatic events (Pitcher, 1983; Zhao *et al.* 2012, 2013). For instance, adakites are usually generated by the partial melting of subducted oceanic crust (Defant & Drummond, 1990; Castillo, 2006), and small amounts of co-subduction granites may be generated during the deep subduction of continental crust (Zheng *et al.* 2011; Zhang *et al.* 2015), while large-scale magmatic events always occur along with exhumation of the subducted plate (Zheng, 2012). The extension and collapse of the thickened orogenic belt in the post-orogenic stage may form vast amounts of granitic rocks by partial melting of the lower crust triggered by the upwelling of basaltic magma (Bonin, 2004; Li *et al.* 2013; Song *et al.* 2014; Wang *et al.* 2014).

The Altyn orogenic belt (AOB) is an important subduction–collision complex in NW China, extending more than 1000 km to the NE and connecting the southern margin of the Tarim Basin and the northern margin of the Qaidam Basin (QB; Fig. 1b). The AOB records tectonic–magmatic events in the Neoproterozoic to the mid-Palaeozoic (Han *et al.* 2012; Guo *et al.* 2015; Zhang *et al.* 2016), and underwent a complicated evolution including formation of the Archaean–Palaeoproterozoic continental nucleus and crystalline basement (Liu *et al.* 1998; Xu *et al.* 1999), Mesoproterozoic stable continental-margin deposition, Neoproterozoic plate rifting (Zhang *et al.* 2010, 2017; Wu *et al.* 2018), and early Palaeozoic plate subduction–collision (Liu *et al.* 1998; Xu *et al.* 1999). These events were followed by late Palaeozoic denudation–peneplanation, and local shallow-sea deposition (Zhang *et al.* 2010; Yu *et al.* 2019), The Triassic extension, and major sinistral strike-slip occurred during the Late Jurassic to Early Cretaceous, resulting in the construction of a composite orogenic belt, which consists of geological complexes formed at various tectonic levels, and in a wide range of tectonic settings (Zhang *et al.* 2017; Wu *et al.* 2018; Yu *et al.* 2019). Two ophiolite zones, termed as the south and the north Altyn ophiolite zones, are found in the AOB, indicating the occurrence of the North Altyn Ocean and the South Altyn Ocean (SAO) (Yang *et al.* 2002). According to previous regional geological data, the AOB can be divided into five units from the north to the south, e.g. the North Altyn Block (NAB) (Fig. 1b, I), the North Altyn ophiolitic mélange zone (Fig. 1b, II), the Central Altyn Continental Block (CACB) (Fig. 1b, III), the South Altyn Continental Block (SACB) (also termed the Palaeozoic South Altun HP-UHP belt) (Fig. 1b, IV) and the early Palaeozoic Apa–Mangya Ophiolitic Mélange Belt (AMOB) (Fig. 1b, V) (Xu *et al.* 1999; Wu *et al.* 2014, 2016, 2018).

CAMBRIDGE UNIVERSITY PRESS

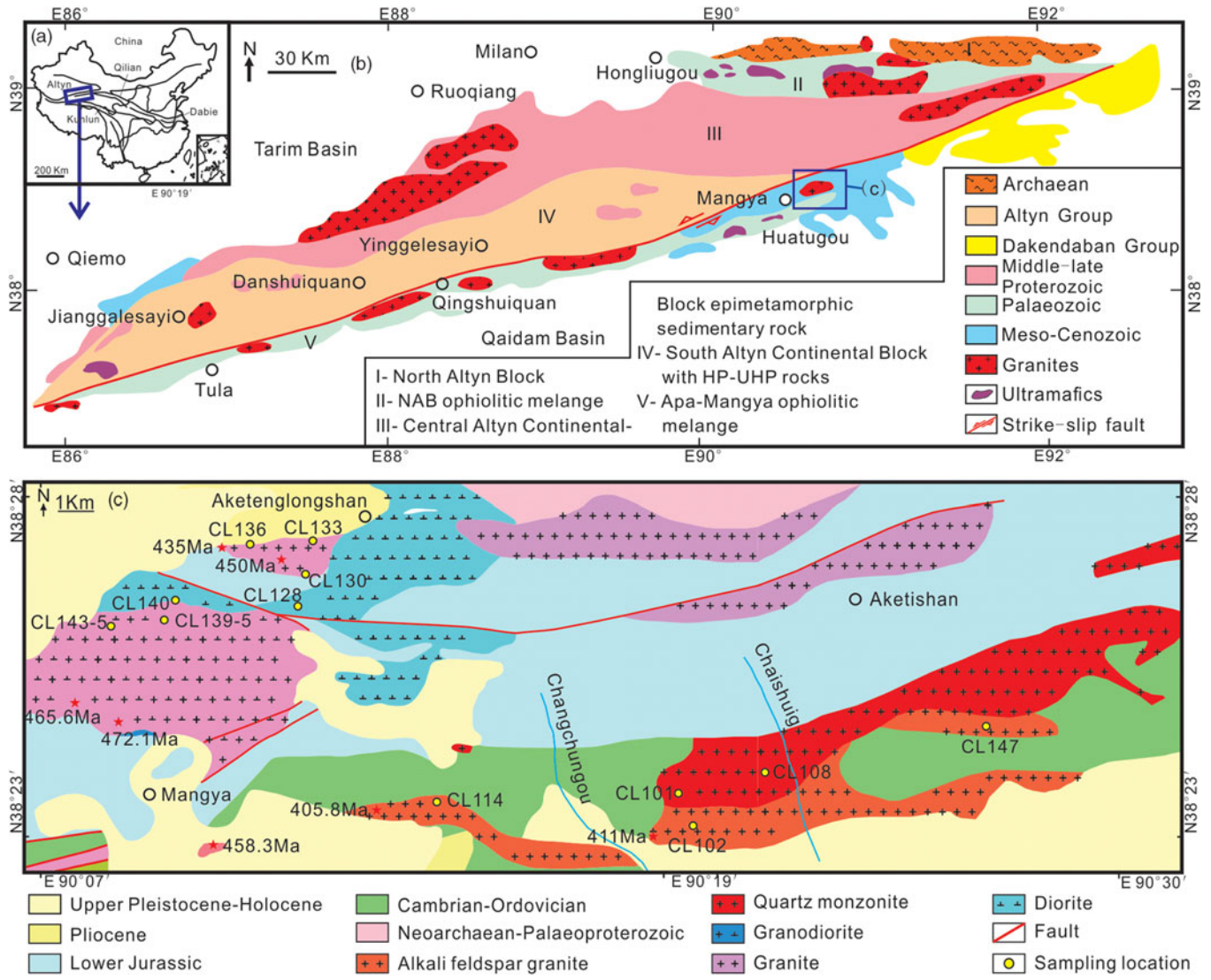

Fig. 1. (Colour online) (a) Map of China showing location of study area. (b) Distribution of granitic rocks in the Altyn Orogenic Belt. (c) Geological map of the Mangya area.

The South Altyn Orogenic Belt (SAOB) consists of the AMOB and the SACB (Fig. 1c), and is an important structural unit in the AOB. Many authors have studied its Palaeozoic tectonic evolution (e.g. Xu *et al.* 1999; L Liu *et al.* 2007*a*, *b*, 2009, 2010, 2012; Ma *et al.* 2009; Cao *et al.* 2013; Kang *et al.* 2014; Wang *et al.* 2014; Wu *et al.* 2014, 2016, 2018; Zhang *et al.* 2017; Yu *et al.* 2019). Previous research indicates that the high-pressure/ultra-high-pressure (HP/UHP) rocks were formed during the deep subduction of the SACB and underwent retrograde metamorphism twice after the peak metamorphism, indicating two episodes of uplift of the SACB after deep subduction (Liu *et al.* 2007*a*, *b*, 2009, 2010, 2012; Ma *et al.* 2009; Cao *et al.* 2013; Kang *et al.* 2014; Wang *et al.* 2014). Many Early Palaeozoic plutons have been discovered in the SAOB, which record key information on mantle–crust interaction, whereas fewer studies have been carried out on these plutons (Liu *et al.* 2002, 2015; Ma *et al.* 2009; Kang *et al.* 2014; Wu *et al.* 2014, 2016, 2018). The Mangya Plutons crop out at the southern margin of the Altyn sinistral strike-slip fault (ASSF), extending more than 20 km in length and 8 km in width (Fig. 1b). These granitic rocks were triggered by different tectonic processes during the Palaeozoic orogeny in the SAOB, e.g. the newly discovered adakitic rocks may provide strong evidence for the subduction of the slab of the SAO, and the A-type granites were generated in the last stage of the orogeny. Thus, the Mangya plutons in this study are the ideal choice to reveal the Palaeozoic tectonic evolution of the SAOB.

The granitic rocks in the SAOB were divided into six episodes: 503–497 Ma, 483–458 Ma, 456–432 Ma, 424–385 Ma, 352–338 Ma and 265–264 Ma. The first and second plutonic episodes were triggered by the subduction of the oceanic crust of the SAO; the third episode was generated in post-collision setting; the fourth episode was formed in post-orogenic extensional environment; the fifth episode was related to the subduction of the Palaeo Tethys and the Palaeo Asian oceans, and the crust of the Altyn and Qilian orogenic belt thickened in this period; the sixth episode resulted from the reactivation of the ASSF (Wu *et al.* 2014, 2016, 2018). Another model proposes that: at >517 Ma (granitic rocks, laser ablation inductively coupled plasma mass spectrometer (LA-ICP-MS); Kang *et al.* 2016), the oceanic crust began sinking, and some adakites were generated by the partial melting of the continental lithospheric mantle; during 504–487 Ma (eclogite, LA-ICP-MS; Liu *et al.* 2015), the deep subduction of the continental crust occurred;

https://doi.org/10.1017/S0016756820000126 Published online by Cambridge University Press

from 451 to 462 Ma (eclogite, LA-ICP-MS; Liu *et al.* 2015), the break-off and exhumation of the subducted continental crust occurred; and during 426–385 Ma (granites, LA-ICP-MS; Wu *et al.* 2014, 2018), the SAOB was in post-orogenic extensional environment (Liu *et al.* 1999, 2012, 2015).

However, debate still remains: How many episodes of granitic magmatism occurred during the Palaeozoic in the AMOB, and what kind of tectonic setting is represented by each episode? When did the subduction of the SAO and the deep subduction of the continental crust initiate? To deal with these questions, here, we present new data from zircon U–Pb geochronological, Lu–Hf isotopic and whole-rock geochemical data of the Mangya plutons with a view to deciphering the early Palaeozoic magmatism and the dynamic processes in the SAOB.

2. Geological setting

The AOB is composed of HP/UHP metamorphic rocks, ophiolites, and magmatic rocks belonging to different orogenic stages and tectonic settings (Xu *et al.* 1999; L Liu *et al.* 2010, 2012, 2015; Wu *et al.* 2014, 2016, 2018). The SACB lies between the CACB and the ASSF, and is composed of amphibolite-facies felsic gneiss, marbles and mafic amphibolites (Liu *et al.* 2012, 2015). The HP/UHP rocks in the SACB include eclogite, pelitic gneiss, garnet iherzolite, garnet pyroxenite and granitic gneiss, which are exposed in the Jianggalasayi, Qingshuiquan and Yinggelesayi areas, extending more than 200 km (Fig. 1b). The UHP rocks (eclogite) underwent granulite (~450 Ma) and amphibolites-facies retrograde metamorphism after peak metamorphism (~500 Ma) (L Liu *et al.* 2009, 2010, 2012, 2015). The AMOB extends almost 700 km along the southern margin of the ASSF (Fig. 1b, -V), and is composed of Early Palaeozoic ophiolites, mafic–ultramafic rocks, and late Tonian to early Cambrian deposits.

The geological units in the Mangya area include Cambrian–Ordovician greyish-green tuff sandstones, which were intruded by alkali feldspar granites and quartz monzonites (Fig. 1c). The Neoarchaean–Palaeoproterozoic formations and the Palaeozoic granitic rocks are mostly overlain by Mesozoic–Cenozoic formations (Fig. 1c). The granitoid associations are alkali feldspar granite, quartz monzonite, quartz monzodiorite, granodiorite, diorite and monzonitic granites. According to our field investigation, the alkali feldspar granites and quartz monzonites locate at the SE of the research area, and both plutons are 1.5–2 km in width and 15–20 km in length, extending roughly in an E–W direction (Fig. 1c). The diorites locate at both sides of the E–W-trending fault, and the monzonitic granites locate at the west of the north-side diorites, while the quartz monzodiorites and granodiorites locate at the south of the south-side diorites (Fig. 1c). The alkali feldspar granites intrude into the quartz monzonites. The quartz monzodiorites and granodiorites are mostly overlain by Mesozoic–Cenozoic formations, so their relationship is difficult to observe. The north-side diorites are intruded by the monzonitic granites, and the south-side diorites are intruded by the quartz monzodiorites and granodiorites.

3. Sampling and analytical techniques

Twelve fresh samples were collected from the Mangya plutons for geochemical, zircon U–Pb and Hf isotopic analyses in this study, including samples CL101, CL108, CL128, CL140, CL143-5, CL139, CL130, CL133, CL136, CL102, CL114 and CL147. The sample location and numbers are shown in Figure 1c.

3.a Major and trace elements

Twelve samples were collected for whole-rock geochemical analyses at the Hebei Institute of Regional Geological and Mineral Resource Survey, Langfang, Hebei Province, China. Oxide concentrations were measured using a 3080 E X-ray fluorescence spectrometer. Na_2O, MgO, Al_2O_3, SiO_2, P_2O_5, K_2O, CaO, TiO_2, MnO, Fe_2O_3 and FeO content determinations were based on the GB/T14506. 28 1993 standard, and H_2O^+, CO_2 and loss on ignition (LOI) on GB/T14506. 2-1993, GB9835-1988 and LY/T1253-1999. The relative standard deviations were lower than 2–8 %. Rare earth elements (REEs: La, Ce, Pr, Nd, Sm, Eu, Gd, Tb, Dy, Ho, Er, Tm, Yb, Lu and Y) and trace elements (Cu, Pb, Hf, Ta, Sc, Cs, V, Co and Ni) were analysed using an ICP-MS (PlasmaQuad Excell) with JY/T016-1996 as the executive standard. The precision for most elements was 10^{-8}, while that of Zr and Ba was 10^{-6} and that for Hf and Nb was 10^{-7}. The relative standard deviations were less than 10 %. The analytical results are listed in Table 1.

3.b Zircon U–Pb dating

Zircon U–Pb analyses were performed using an LA-MC (multi-collector)-ICP-MS apparatus at the Institute of Geology, Chinese Academy of Geological Sciences, and detailed procedures were according to Hou *et al.* (2007). The spots were ~32 μm in size, while the data were calibrated by the reference zircon, M127 (Nasdala *et al.* 2008). Standard zircon was analysed initially and repeated after every five spots. Reference standards were the GJ-1 zircon (599.8 ± 1.7 Ma (2σ); Jackson *et al.* 2004) and the Plesovice zircon (337.13 ± 0.37 Ma (2σ); Sláma *et al.* 2008). The ICPMSDataCal program was used for data processing (Liu *et al.* 2010). Most analysis spots with $^{206}Pb/^{204}Pb > 1{,}000$ were not corrected for common lead. Analyses with unusually high ^{204}Pb were excluded from the calculations because common lead in inclusions was assumed to have affected the data. The analytical data are listed in Supplementary Table S1 in Supplementary Material available online at https://doi.org/10.1017/S0016756820000126 and graphically plotted on Concordia diagrams with 1σ error. The weighted mean ages are calculated using Isoplot (Ludwig, 2003) with 1σ errors at 95 % confidence.

3.c Hf isotopic analyses

In situ zircon Hf isotope analyses were performed using a GeoLasPro 193 nm laser-ablation microprobe attached to a Neptune MC-ICP-MS at the Institute of Geology, Chinese Academy of Geological Sciences. Instrumental and data acquisition conditions were according to Hou *et al.* (2007). A stationary spot was used for the analysis, with a beam diameter of 44 μm, depending on the size of the ablated domains. Helium was used as the carrier gas to transport the ablated samples from the laser-ablation cell to the ICP-MS torch via a mixing chamber filled with argon. To correct the isobaric interferences from ^{176}Lu and ^{176}Yb on ^{176}Hf, the $^{176}Lu/^{175}Lu = 0.02658$ and $^{176}Yb/^{173}Yb = 0.796218$ ratios were determined (Chu *et al.* 2002). For instrumental mass bias corrections, an exponential law was applied to normalize the Yb and Hf isotope ratios to a $^{172}Yb/^{173}Yb$ ratio of 1.35274 (Chu *et al.* 2002) and to a $^{179}Hf/^{177}Hf$ ratio of 0.7325. The mass bias behaviour of Lu was assumed to follow that of Yb. Mass bias correction protocol details have been described in detail by Hou *et al.* (2007). Zircon GJ-1 was used as the reference standard during routine analyses, with a weighted mean $^{176}Hf/^{177}Hf$ ratio of 0.282007 ± 0.000007 (2σ) that was indistinguishable from the weighted mean $^{176}Hf/^{177}Hf$ ratio of

https://doi.org/10.1017/S0016756820000126 Published online by Cambridge University Press

Table 1. Major and trace elements concentrations and ratios of the samples in this study

Sample No.	CL101	CL108	CL140	CL128	CL143-5	CL139	CL130	CL133	CL136	CL102	CL114	CL147
Maior elements (wt %)												
SiO_2	57.97	58.68	58.79	58.30	75.67	64.16	75.68	72.60	73.93	76.81	78.53	77.07
TiO_2	0.77	0.94	1.99	0.32	0.15	0.76	0.16	0.25	0.10	0.15	0.07	0.16
Al_2O_3	14.62	15.07	12.59	17.72	12.97	15.78	13.40	14.30	14.37	11.92	11.37	11.90
Fe_2O_3	5.23	3.51	2.50	1.19	0.31	1.89	0.15	0.64	0.27	0.91	0.37	0.80
FeO	3.60	3.62	2.72	3.45	0.82	3.08	0.75	1.37	0.60	0.31	0.38	0.45
MnO	0.18	0.14	0.09	0.09	0.02	0.07	0.01	0.06	0.02	0.03	0.02	0.04
MgO	3.13	3.54	5.87	4.75	0.75	2.03	0.34	0.49	0.48	0.14	0.12	0.11
CaO	4.70	4.80	4.16	6.89	3.29	2.93	0.40	1.03	1.61	0.34	0.54	0.51
Na_2O	3.49	2.89	3.10	2.56	2.91	3.40	3.46	3.21	3.71	3.73	3.17	3.58
K_2O	3.73	3.95	2.75	1.37	1.57	2.58	4.70	4.52	3.56	5.15	4.74	4.72
P_2O_5	0.35	0.41	0.20	0.07	0.02	0.29	0.02	0.10	0.05	0.01	0.01	0.02
H_2O^+	1.39	1.66	1.48	2.35	0.84	2.02	0.68	0.97	0.74	0.13	0.23	0.37
H_2O^-	0.19	0.13	0.57	0.19	0.13	0.23	0.13	0.15	0.12	0.08	0.08	0.12
LOI	0.96	0.14	0.98	0.14	1.12	0.63	0.82	1.08	1.00	0.45	0.60	0.53
Total	99.72	99.70	99.76	99.85	99.60	99.60	99.91	99.65	99.70	99.95	99.93	99.88
$Na_2O + K_2O$	7.22	6.85	3.85	3.94	4.49	5.97	8.16	7.73	7.26	8.89	7.91	8.30
Na_2O/K_2O	0.94	0.73	1.20	1.87	1.85	1.32	0.74	0.71	1.04	0.73	0.67	0.76
Fe*	0.73	0.63	0.57	0.49	0.59	0.70	0.72	0.80	0.64	0.89	0.85	0.91
Trace elements (ppm)												
Li	16.15	16.12	62.82	28.38	1.75	18.45	10.85	21.63	19.45	2.73	4.20	3.89
Be	3.88	3.59	1.50	1.51	1.70	3.11	3.19	4.01	1.06	3.10	2.27	4.62
Sc	10.36	11.45	25.51	15.01	6.44	14.39	4.80	8.24	7.05	4.49	5.85	5.78
V	120.47	143.77	255.81	60.10	26.68	79.02	10.35	19.92	15.46	2.92	2.74	3.21
Cr	56.35	104.28	10.57	112.69	9.64	16.85	8.07	3.12	6.82	3.46	3.30	2.58
Co	17.35	23.27	34.27	19.74	4.67	12.53	1.23	2.60	2.54	0.57	1.77	0.43
Ni	28.81	44.30	44.50	52.60	8.66	12.08	1.96	3.01	2.66	1.28	1.53	1.03
Cu	33.86	8.54	40.33	16.05	15.46	21.25	1.51	2.16	3.03	1.82	1.37	3.32
Zn	98.24	79.10	89.22	67.14	16.72	89.64	14.71	33.49	15.05	41.42	11.12	46.96
Ga	19.54	17.58	24.87	20.04	13.19	23.44	14.23	17.88	16.62	15.98	11.96	21.18
Rb	152	162	98	76	48	128	212	182	106	169	200	169
Sr	399	392	1140	605	566	428	164	337	333	18	42	24
Zr	361	290	132	122	261	307	113	190	149	175	66	236
Nb	28.28	24.74	20.31	10.16	4.07	25.95	21.41	20.67	4.90	25.34	21.23	28.63
Mo	0.83	0.67	0.63	0.25	0.48	0.63	0.09	0.29	0.01	0.55	0.07	0.94
Cd	0.15	0.15	0.06	0.06	0.02	0.04	0.01	0.02	0.02	0.05	0.02	0.10
In	0.07	0.07	0.10	0.03	0.01	0.05	0.01	0.04	0.02	0.05	0.01	0.06
Cs	3.67	4.02	3.83	2.95	1.35	4.16	7.11	5.61	5.75	4.65	6.46	2.68
Ba	1355	1392	338	189	617	677	263	967	917	146	233	186
Hf	9.99	8.18	3.91	3.43	8.16	7.65	3.64	5.33	4.28	6.71	2.79	9.16
Ta	2.07	1.23	1.09	0.67	0.20	1.26	2.94	1.99	0.51	1.90	3.48	1.43
W	0.71	0.93	0.43	0.15	0.10	0.22	0.45	0.31	0.30	1.60	0.56	1.07
Tl	0.99	0.95	0.45	0.47	0.29	0.67	1.26	1.06	0.62	0.95	1.18	0.97

(*Continued*)

https://doi.org/10.1017/S0016756820000126 Published online by Cambridge University Press

Table 1. (*Continued*)

Sample No.	CL101	CL108	CL140	CL128	CL143-5	CL139	CL130	CL133	CL136	CL102	CL114	CL147
Pb	32.12	33.69	9.79	10.25	16.77	17.93	33.18	34.00	36.43	25.67	31.02	29.16
Bi	0.13	0.20	0.04	0.02	0.01	0.02	0.01	0.17	0.14	0.13	0.16	0.14
Th	24.95	16.75	7.79	16.40	100.96	20.37	23.07	27.27	16.92	16.87	15.90	15.73
U	4.16	3.32	2.22	1.99	4.04	2.46	2.11	2.40	2.31	1.66	3.02	2.81
Th/Ta	12.04	13.60	10.04	24.48	510.01	16.12	7.84	13.73	33.35	8.86	4.57	11.02
Rare earth elements (ppm)												
Y	32.01	23.20	28.63	6.89	2.42	19.05	11.52	16.93	19.96	34.40	47.18	68.65
La	76.25	51.88	43.70	13.06	8.01	76.01	6.67	49.12	32.18	38.17	113.82	50.01
Ce	139.69	116.53	102.40	24.17	12.61	136.46	11.36	86.07	58.11	76.80	229.79	108.44
Pr	15.53	14.29	14.37	2.28	1.01	14.51	1.19	9.21	6.61	10.14	22.35	14.50
Nd	68.04	53.28	58.02	7.99	3.16	46.19	4.35	29.25	22.23	38.66	79.95	54.56
Sm	11.33	9.10	10.99	1.40	0.44	6.56	1.05	4.46	4.40	7.45	16.20	12.04
Eu	2.59	2.31	3.05	0.64	0.84	1.54	0.43	1.07	1.34	0.58	0.73	0.69
Gd	9.63	7.60	8.41	1.21	0.43	6.12	1.09	4.13	4.11	6.88	15.24	10.95
Tb	1.38	1.06	1.21	0.18	0.05	0.72	0.24	0.56	0.69	1.20	2.41	2.10
Dy	6.55	4.94	6.26	1.05	0.30	3.36	1.68	2.97	3.75	7.07	12.02	13.77
Ho	1.19	0.89	1.05	0.20	0.06	0.60	0.35	0.52	0.59	1.40	2.20	2.71
Er	3.35	2.37	2.86	0.59	0.23	1.72	1.06	1.44	1.45	3.97	5.81	7.73
Tm	0.48	0.34	0.40	0.10	0.05	0.23	0.19	0.22	0.19	0.63	0.83	1.23
Yb	3.03	2.30	2.39	0.66	0.37	1.43	1.27	1.44	1.07	4.04	4.92	7.51
Lu	0.47	0.39	0.36	0.12	0.08	0.23	0.21	0.24	0.17	0.64	0.73	1.18
TREE	339.51	267.28	255.48	53.65	27.65	295.69	31.14	190.69	136.88	197.63	506.99	287.41
LREE	313.43	247.39	232.53	49.54	26.07	281.27	25.04	179.18	124.86	171.80	462.84	240.25
HREE	26.08	19.90	22.95	4.12	1.58	14.42	6.10	11.52	12.03	25.83	44.14	47.17
LREE/HREE	12.02	12.43	10.13	12.03	16.53	19.50	4.11	15.56	10.38	6.65	10.48	5.09
La_N/Yb_N	18.03	16.21	13.13	14.14	15.49	38.14	3.77	24.41	21.57	6.77	16.60	4.78
Eu*	0.74	0.83	0.93	1.48	5.82	0.73	1.22	0.75	0.95	0.24	0.14	0.18
Ce*	0.94	1.03	1.00	1.00	0.93	0.94	0.91	0.92	0.92	0.94	1.05	0.97

0.282000 ± 0.000005 (2σ). The Hf model age (single-stage model age) (TDM) was calculated on the basis of a depleted-mantle source with a present-day $^{176}Hf/^{177}Hf$ ratio of 0.28325 by using the ^{176}Lu decay constant, 1.865×10^{-11} a^{-1} (Scherer *et al.* 2001). The crust (two-stage) Hf model age (TDMC) was calculated based on the assumption of a mean $^{176}Lu/^{177}Hf$ value of 0.015 for an average continental crust (Griffin *et al.* 2002). Analytical results are listed in Table 2.

4. Petrography and results

4.a Petrography

The petrographic features of the samples are shown in Table 3.

4.b Chronology

Ten samples were collected for LA-ICP-MS zircon U–Pb dating, including samples CL101 and CL108 (quartz monzonite), CL140 (diorite), CL128 (diorite), CL139 (quartz monzodiorite), CL143-5 (granodiorite), CL136 and CL137 (monzonitic granite), CL102 and CL147 (alkali feldspar granite). The analytical results are shown in Supplementary Table S1 in Supplementary Material available online at https://doi.org/10.1017/S0016756820000126.

The trace element composition of zircon varies significantly according to formation process (crystallization vs recrystallization) and fluid/melt involved. Zircon overgrowths crystallized during high-temperature metamorphism in equilibrium with partial melt have compositions similar to magmatic zircon, i.e. rich in U, Y, Hf and P, displaying steep REE patterns with positive Ce anomalies and negative Eu anomalies. Their low Th/U ratio (<0.07) is the only chemical feature that distinguishes them from magmatic zircon (Rubatto, 2002). The ratios of Th/U are 1:3 and 1:7 in felsic melts and mafic melts, respectively, implying that mafic melts do not allow relatively more Th into the zircon structure than U, but both more U and Th (Kirkland *et al.* 2015). This is consistent with crystal chemical theory, where relatively more elements with larger ionic radii

https://doi.org/10.1017/S0016756820000126 Published online by Cambridge University Press

Table 2. Zircon Lu–Hf isotopic data of Mangya plutons

Sample	Age (Ma)	$^{176}Hf/^{177}Hf$	2σ	$^{176}Lu/^{177}Hf$	2σ	$^{176}Yb/^{177}Hf$	2σ	$\epsilon_{Hf}(0)$	$\epsilon_{Hf}(T)$	2σ	TDM1	TDM2	fLu/Hf(s)
CL101-01	504	0.282417	0.000021	0.000955	0.000005	0.036045	0.000087	−12.57	−1.79	0.73	1179	1584	−0.97
CL101-02	514	0.282469	0.000024	0.001218	0.000010	0.045556	0.000654	−10.71	0.19	0.86	1113	1466	−0.96
CL101-03	506	0.282442	0.000021	0.001139	0.000003	0.042502	0.000188	−11.68	−0.91	0.73	1149	1530	−0.97
CL101-04	502	0.282442	0.000025	0.001064	0.000011	0.040561	0.000668	−11.67	−0.97	0.89	1147	1531	−0.97
CL101-05	513	0.282419	0.000025	0.000798	0.000033	0.030231	0.001163	−12.50	−1.48	0.89	1171	1571	−0.98
CL101-06	515	0.282425	0.000020	0.001433	0.000009	0.056358	0.000707	−12.26	−1.41	0.70	1182	1568	−0.96
CL101-07	520	0.282450	0.000025	0.001151	0.000040	0.043506	0.001747	−11.39	−0.32	0.87	1138	1504	−0.97
CL101-08	505	0.282461	0.000023	0.000582	0.000009	0.021767	0.000376	−11.00	−0.08	0.82	1106	1476	−0.98
CL101-09	518	0.282404	0.000023	0.000780	0.000008	0.028723	0.000525	−13.02	−1.88	0.83	1191	1601	−0.98
CL101-10	510	0.282498	0.000024	0.001018	0.000003	0.040875	0.000160	−9.70	1.19	0.85	1067	1400	−0.97
CL108-01	481	0.282420	0.000017	0.000780	0.000007	0.029445	0.000250	−12.44	−2.09	0.62	1169	1586	−0.98
CL108-02	498	0.282435	0.000017	0.000820	0.000022	0.030065	0.000879	−11.91	−1.21	0.62	1149	1543	−0.98
CL108-03	487	0.282402	0.000015	0.000818	0.000013	0.030952	0.000374	−13.09	−2.64	0.54	1195	1625	−0.98
CL108-04	478	0.282445	0.000015	0.000820	0.000010	0.030614	0.000404	−11.56	−1.29	0.55	1135	1533	−0.98
CL108-05	481	0.282414	0.000016	0.000909	0.000013	0.033762	0.000641	−12.67	−2.36	0.58	1181	1603	−0.97
CL108-06	476	0.282428	0.000016	0.000914	0.000004	0.032878	0.000394	−12.16	−1.31	0.56	1153	1553	−0.97
CL108-07	502	0.282411	0.000016	0.000614	0.000004	0.022122	0.000077	−12.16	−1.31	0.56	1153	1553	−0.98
CL108-08	509	0.282378	0.000018	0.001016	0.000005	0.037200	0.000217	−12.78	−1.92	0.58	1189	1596	−0.97
CL108-09	500	0.282421	0.000017	0.001266	0.000019	0.047113	0.000883	−13.92	−3.33	0.63	1243	1679	−0.96
CL108-10	496	0.282409	0.000019	0.001336	0.000008	0.048732	0.000188	−12.42	−1.94	0.59	1185	1587	−0.96
CL108-11	512	0.282419	0.000018	0.001105	0.000015	0.042395	0.000675	−12.84	−1.95	0.67	1195	1600	−0.97
CL108-12	505	0.282454	0.000019	0.001209	0.000015	0.044567	0.000702	−12.48	−1.76	0.63	1183	1583	−0.96
CL108-13	505	0.282410	0.000018	0.000630	0.000006	0.023110	0.000121	−11.25	−0.35	0.68	1117	1494	−0.98
CL108-14	501	0.282429	0.000016	0.000769	0.000002	0.028718	0.000282	−12.82	−2.05	0.64	1183	1598	−0.98
CL108-15	480	0.282449	0.000016	0.000753	0.000005	0.027654	0.000226	−12.12	−1.79	0.55	1155	1566	−0.98
CL108-16	487	0.282411	0.000018	0.000842	0.000008	0.031264	0.000347	−11.41	−0.96	0.55	1130	1519	−0.97
CL108-17	504	0.282423	0.000019	0.001188	0.000014	0.044494	0.000699	−12.78	−2.08	0.63	1195	1602	−0.96
CL108-18	503	0.282439	0.000019	0.000912	0.000009	0.034655	0.000211	−12.33	−1.56	0.66	1168	1569	−0.97
CL108-19	506	0.282469	0.000019	0.001113	0.000034	0.041172	0.001054	−11.76	−0.99	0.68	1152	1535	−0.97
CL108-20	500	0.282452	0.000016	0.000674	0.000007	0.024989	0.000336	−10.73	0.06	0.68	1098	1464	−0.98
CL108-21	480	0.282445	0.000019	0.000784	0.000003	0.029360	0.000108	−11.57	−1.24	0.68	1134	1532	−0.98
CL108-22	498	0.282443	0.000017	0.000654	0.000013	0.024248	0.000553	−11.64	−0.90	0.62	1133	1523	−0.98
CL108-23	487	0.282424	0.000019	0.000588	0.000004	0.021849	0.000057	−12.32	−1.80	0.68	1158	1572	−0.98
CL108-24	491	0.282435	0.000018	0.000497	0.000005	0.018417	0.000120	−11.92	−1.28	0.65	1140	1542	−0.99
CL108-25	480	0.282406	0.000015	0.000797	0.000006	0.029368	0.000325	−12.95	−2.64	0.54	1189	1620	−0.98
CL108-26	475	0.282412	0.000018	0.001007	0.000009	0.037785	0.000417	−12.74	−2.60	0.63	1187	1613	−0.97
CL108-27	474	0.282427	0.000019	0.000639	0.000011	0.023792	0.000514	−12.18	−1.95	0.68	1154	1572	−0.98
CL108-28	478	0.282454	0.000018	0.001077	0.000007	0.040482	0.000223	−11.25	−1.06	0.64	1131	1519	−0.97
CL108-29	476	0.282413	0.000017	0.000405	0.000001	0.015292	0.000055	−12.69	−2.33	0.59	1167	1598	−0.99
CL108-30	487	0.282468	0.000021	0.001500	0.000015	0.059122	0.000661	−10.74	−0.51	0.73	1123	1490	−0.95
CL108-31	474	0.282383	0.000017	0.000583	0.000002	0.021917	0.000090	−13.76	−3.51	0.61	1214	1670	−0.98
CL108-32	480	0.282419	0.000020	0.000830	0.000022	0.031026	0.000993	−12.48	−2.17	0.69	1172	1590	−0.98
CL140-01	495	0.282531	0.000021	0.000184	0.000008	0.005631	0.000336	−8.51	2.33	0.74	998	1316	−0.99

(*Continued*)

https://doi.org/10.1017/S0016756820000126 Published online by Cambridge University Press

Table 2. (*Continued*)

Sample	Age (Ma)	$^{176}Hf/^{177}Hf$	2σ	$^{176}Lu/^{177}Hf$	2σ	$^{176}Yb/^{177}Hf$	2σ	$\epsilon_{Hf}(0)$	$\epsilon_{Hf}(T)$	2σ	TDM1	TDM2	fLu/Hf(s)
CL140-02	500	0.282556	0.000019	0.000285	0.000008	0.008795	0.000206	−7.63	3.29	0.67	966	1259	−0.99
CL140-03	500	0.282546	0.000019	0.000566	0.000001	0.021185	0.000096	−8.00	2.83	0.67	988	1289	−0.98
CL140-04	486	0.282559	0.000024	0.000281	0.000002	0.009644	0.000092	−7.52	3.09	0.83	962	1261	−0.99
CL140-05	498	0.282527	0.000024	0.000610	0.000006	0.023142	0.000318	−8.66	2.11	0.84	1015	1333	−0.98
CL140-06	488	0.282562	0.000021	0.001149	0.000006	0.044647	0.000090	−7.42	2.97	0.74	980	1271	−0.97
CL140-07	487	0.282511	0.000018	0.000346	0.000003	0.012975	0.000181	−9.22	1.40	0.65	1030	1370	−0.99
CL140-08	497	0.282513	0.000018	0.000607	0.000004	0.023329	0.000072	−9.16	1.60	0.65	1034	1365	−0.98
CL140-09	491	0.282582	0.000017	0.000641	0.000003	0.022188	0.000054	−6.71	3.90	0.59	939	1214	−0.98
CL140-10	496	0.282569	0.000016	0.000516	0.000005	0.018411	0.000267	−7.18	3.57	0.57	954	1238	−0.98
CL140-11	496	0.282518	0.000018	0.000425	0.000013	0.014781	0.000597	−8.97	1.82	0.64	1022	1350	−0.99
CL140-12	491	0.282550	0.000016	0.000443	0.000002	0.015468	0.000127	−7.87	2.80	0.58	979	1283	−0.99
CL140-13	490	0.282575	0.000015	0.000544	0.000001	0.018046	0.000070	−6.96	3.65	0.52	946	1229	−0.98
CL140-14	489	0.282507	0.000015	0.000489	0.000022	0.014698	0.000638	−9.37	1.24	0.53	1040	1381	−0.99
CL140-15	492	0.282560	0.000016	0.000350	0.000002	0.012208	0.000022	−7.51	3.22	0.57	963	1258	−0.99
CL140-16	497	0.282538	0.000016	0.000419	0.000003	0.015271	0.000069	−8.28	2.53	0.57	995	1305	−0.99
CL140-17	496	0.282524	0.000016	0.000375	0.000002	0.013720	0.000119	−8.76	2.03	0.56	1013	1336	−0.99
CL140-18	494	0.282529	0.000015	0.000205	0.000002	0.006352	0.000075	−8.61	2.20	0.54	1002	1324	−0.99
CL140-19	497	0.282560	0.000019	0.001134	0.000002	0.041696	0.000054	−7.48	3.09	0.69	982	1270	−0.97
CL140-20	504	0.282545	0.000014	0.000187	0.000005	0.005898	0.000185	−8.03	3.01	0.50	979	1280	−0.99
CL128-01	478	0.282491	0.000017	0.000592	0.000003	0.019989	0.000168	−9.95	0.39	0.61	1065	1427	−0.98
CL128-02	482	0.282502	0.000016	0.000922	0.000001	0.030545	0.000173	−9.57	0.75	0.58	1059	1407	−0.97
CL128-03	482	0.282456	0.000015	0.000318	0.000005	0.010729	0.000133	−11.18	−0.66	0.54	1105	1496	−0.99
CL128-04	483	0.282529	0.000017	0.000642	0.000005	0.021352	0.000089	−8.59	1.85	0.59	1013	1338	−0.98
CL128-05	490	0.282475	0.000018	0.001445	0.000004	0.050766	0.000397	−10.49	−0.18	0.65	1111	1471	−0.96
CL128-06	489	0.282493	0.000017	0.000387	0.000001	0.011429	0.000068	−9.85	0.78	0.59	1056	1410	−0.99
CL128-07	479	0.282493	0.000013	0.000509	0.000004	0.017139	0.000080	−9.86	0.52	0.47	1059	1419	−0.98
CL128-08	480	0.282492	0.000015	0.001155	0.000010	0.039048	0.000381	−9.89	0.32	0.52	1079	1433	−0.97
CL128-09	485	0.282494	0.000018	0.000853	0.000003	0.027629	0.000147	−9.84	0.56	0.64	1068	1421	−0.97
CL128-10	481	0.282491	0.000011	0.000413	0.000003	0.013175	0.000060	−9.95	0.52	0.38	1060	1421	−0.99
CL128-11	494	0.282501	0.000016	0.000383	0.000002	0.011218	0.000097	−9.60	1.16	0.57	1046	1390	−0.99
CL128-12	488	0.282546	0.000018	0.001250	0.000030	0.040775	0.000782	−7.98	2.36	0.62	1005	1309	−0.96
CL128-13	485	0.282506	0.000016	0.000568	0.000006	0.016072	0.000205	−9.39	1.10	0.58	1043	1387	−0.98
CL128-14	481	0.282499	0.000016	0.000299	0.000005	0.008441	0.000098	−9.65	0.84	0.58	1045	1400	−0.99
CL128-15	480	0.282482	0.000015	0.000379	0.000005	0.011853	0.000203	−10.24	0.21	0.52	1071	1439	−0.99
CL128-16	481	0.282522	0.000014	0.000924	0.000003	0.031530	0.000044	−8.84	1.46	0.50	1030	1361	−0.97
CL128-17	478	0.282490	0.000016	0.000466	0.000011	0.014046	0.000379	−9.98	0.39	0.56	1063	1426	−0.99
CL128-18	482	0.282473	0.000016	0.000356	0.000004	0.011351	0.000125	−10.56	−0.06	0.56	1083	1458	−0.99
CL128-19	484	0.282481	0.000013	0.001018	0.000009	0.034554	0.000264	−10.29	0.04	0.47	1090	1453	−0.97
CL128-20	492	0.282501	0.000015	0.000825	0.000009	0.025422	0.000477	−9.58	0.98	0.54	1057	1400	−0.98
CL128-21	484	0.282494	0.000015	0.001483	0.000009	0.053835	0.000489	−9.82	0.37	0.55	1085	1432	−0.96
CL128-22	491	0.282492	0.000017	0.000452	0.000001	0.012962	0.000034	−9.91	0.76	0.60	1060	1413	−0.99
CL128-23	482	0.282495	0.000014	0.000391	0.000005	0.012694	0.000148	−9.79	0.69	0.51	1053	1410	−0.99
CL139-01	475	0.282484	0.000017	0.000681	0.000004	0.026239	0.000204	−10.19	0.05	0.60	1077	1446	−0.98

(*Continued*)

https://doi.org/10.1017/S0016756820000126 Published online by Cambridge University Press

Table 2. (*Continued*)

Sample	Age (Ma)	$^{176}Hf/^{177}Hf$	2σ	$^{176}Lu/^{177}Hf$	2σ	$^{176}Yb/^{177}Hf$	2σ	$\epsilon_{Hf}(0)$	$\epsilon_{Hf}(T)$	2σ	TDM1	TDM2	fLu/Hf(s)
CL139-02	457	0.282510	0.000014	0.000895	0.000035	0.031486	0.001298	−9.27	0.52	0.49	1047	1402	−0.97
CL139-03	471	0.282489	0.000014	0.000469	0.000002	0.015329	0.000056	−10.01	0.22	0.51	1064	1432	−0.99
CL139-04	469	0.282514	0.000015	0.000798	0.000004	0.029881	0.000207	−9.12	0.96	0.53	1038	1383	−0.98
CL139-05	471	0.282521	0.000016	0.001040	0.000017	0.037824	0.000734	−8.88	1.17	0.55	1035	1372	−0.97
CL139-06	481	0.282490	0.000017	0.001672	0.000090	0.059422	0.003125	−9.96	0.09	0.62	1097	1447	−0.95
CL139-07	461	0.282547	0.000013	0.000875	0.000021	0.029160	0.000784	−7.96	1.92	0.45	994	1316	−0.97
CL139-08	471	0.282482	0.000014	0.000412	0.000006	0.013158	0.000231	−10.26	−0.03	0.48	1072	1447	−0.99
CL139-09	469	0.282515	0.000013	0.000755	0.000062	0.025475	0.002120	−9.10	1.00	0.46	1036	1381	−0.98
CL139-10	477	0.282519	0.000015	0.000849	0.000001	0.031427	0.000113	−8.94	1.29	0.54	1032	1368	−0.97
CL139-11	473	0.282574	0.000017	0.001162	0.000023	0.041721	0.000765	−7.02	3.05	0.61	964	1254	−0.97
CL139-12	457	0.282487	0.000013	0.000873	0.000003	0.030112	0.000185	−10.08	−0.28	0.47	1078	1453	−0.97
CL139-13	472	0.282512	0.000014	0.000807	0.000004	0.030165	0.000224	−9.20	0.94	0.51	1042	1387	−0.98
CL139-14	479	0.282480	0.000013	0.000697	0.000003	0.025761	0.000165	−10.32	0.00	0.48	1083	1452	−0.98
CL139-15	464	0.282483	0.000013	0.001068	0.000009	0.033467	0.000151	−10.20	−0.31	0.48	1089	1460	−0.97
CL139-16	471	0.282511	0.000013	0.000783	0.000005	0.028786	0.000244	−9.23	0.90	0.48	1042	1389	−0.98
CL139-17	476	0.282477	0.000013	0.000872	0.000006	0.030704	0.000255	−10.44	−0.24	0.45	1092	1464	−0.97
CL139-18	482	0.282514	0.000014	0.001533	0.000049	0.051788	0.001740	−9.11	1.01	0.49	1058	1390	−0.95
CL139-19	477	0.282523	0.000014	0.000516	0.000016	0.016234	0.000558	−8.80	1.55	0.51	1018	1352	−0.98
CL139-20	473	0.282525	0.000013	0.001164	0.000027	0.035711	0.000664	−8.72	1.33	0.47	1032	1363	−0.96
CL139-21	464	0.282522	0.000014	0.000848	0.000026	0.029167	0.000979	−8.83	1.13	0.48	1028	1369	−0.97
CL143-01	474	0.282536	0.000024	0.001198	0.000020	0.047087	0.000620	−8.35	1.71	0.87	1018	1339	−0.96
CL143-02	483	0.282556	0.000018	0.000918	0.000005	0.032508	0.000162	−7.63	2.71	0.63	982	1283	−0.97
CL143-03	481	0.282512	0.000017	0.000549	0.000004	0.017849	0.000207	−9.19	1.22	0.60	1034	1376	−0.98
CL143-04	484	0.282546	0.000020	0.001021	0.000049	0.040706	0.002300	−8.00	2.34	0.72	1000	1308	−0.97
CL143-05	477	0.282531	0.000017	0.001461	0.000011	0.056852	0.000278	−8.53	1.52	0.62	1033	1354	−0.96
CL143-06	478	0.282499	0.000014	0.000613	0.000008	0.022731	0.000256	−9.67	0.65	0.51	1055	1410	−0.98
CL143-07	479	0.282541	0.000020	0.001029	0.000003	0.041431	0.000182	−8.17	2.06	0.70	1007	1322	−0.97
CL143-08	477	0.282526	0.000018	0.000683	0.000019	0.026573	0.000999	−8.69	1.60	0.65	1018	1349	−0.98
CL143-09	478	0.282525	0.000019	0.000801	0.000021	0.030370	0.000779	−8.74	1.54	0.66	1023	1354	−0.98
CL143-10	481	0.282541	0.000022	0.001136	0.000004	0.043453	0.000227	−8.15	2.09	0.78	1009	1321	−0.97
CL143-11	487	0.282526	0.000019	0.001417	0.000016	0.056361	0.000958	−8.69	1.57	0.66	1038	1358	−0.96
CL143-12	479	0.282545	0.000018	0.000779	0.000070	0.026606	0.002326	−8.01	2.29	0.64	994	1307	−0.98
CL143-13	480	0.282533	0.000019	0.000982	0.000007	0.038101	0.000502	−8.44	1.81	0.67	1016	1338	−0.97
CL143-14	484	0.282538	0.000019	0.001053	0.000011	0.041502	0.000308	−8.27	2.06	0.66	1011	1325	−0.97
CL143-15	489	0.282536	0.000019	0.000928	0.000018	0.034541	0.000916	−8.34	2.12	0.66	1011	1325	−0.97
CL143-16	477	0.282523	0.000015	0.000918	0.000005	0.032229	0.000403	−8.80	1.41	0.54	1029	1361	−0.97
CL143-17	471	0.282545	0.000021	0.000942	0.000018	0.036411	0.000643	−8.02	2.05	0.76	999	1316	−0.97
CL143-18	484	0.282512	0.000017	0.000983	0.000006	0.034163	0.000347	−9.20	1.13	0.59	1046	1383	−0.97
CL143-19	473	0.282511	0.000020	0.000833	0.000023	0.032775	0.001079	−9.23	0.91	0.73	1043	1389	−0.97
CL143-20	474	0.282495	0.000017	0.000731	0.000002	0.028335	0.000085	−9.80	0.41	0.62	1063	1422	−0.98
CL143-21	485	0.282529	0.000019	0.000613	0.000002	0.020246	0.000161	−8.61	1.87	0.67	1013	1338	−0.98
CL137-01	464	0.282482	0.000018	0.001025	0.000022	0.037321	0.000810	−10.25	−0.36	0.64	1089	1463	−0.97
CL137-02	437	0.282536	0.000017	0.001041	0.000016	0.038567	0.000789	−8.34	0.98	0.59	1014	1358	−0.97

(*Continued*)

https://doi.org/10.1017/S0016756820000126 Published online by Cambridge University Press

Table 2. (*Continued*)

Sample	Age (Ma)	$^{176}Hf/^{177}Hf$	2σ	$^{176}Lu/^{177}Hf$	2σ	$^{176}Yb/^{177}Hf$	2σ	$\epsilon_{Hf}(0)$	$\epsilon_{Hf}(T)$	2σ	TDM1	TDM2	fLu/Hf(s)
CL137-03	457	0.282512	0.000016	0.000521	0.000015	0.017661	0.000456	−9.19	0.72	0.56	1033	1390	−0.98
CL137-04	460	0.282519	0.000017	0.001179	0.000008	0.045005	0.000280	−8.96	0.80	0.60	1042	1387	−0.96
CL137-05	438	0.282476	0.000018	0.001524	0.000014	0.057319	0.000237	−10.45	−1.27	0.64	1112	1500	−0.95
CL137-06	440	0.282489	0.000016	0.001294	0.000014	0.049028	0.000712	−10.00	−0.69	0.55	1087	1466	−0.96
CL137-07	455	0.282500	0.000015	0.000293	0.000004	0.009446	0.000095	−9.62	0.31	0.54	1044	1414	−0.99
CL137-08	459	0.282477	0.000017	0.000402	0.000005	0.012405	0.000196	−10.45	−0.46	0.60	1079	1466	−0.99
CL137-09	456	0.282514	0.000021	0.001575	0.000026	0.059193	0.001225	−9.12	0.43	0.76	1060	1406	−0.95
CL137-10	449	0.282494	0.000018	0.000726	0.000021	0.027430	0.000836	−9.83	−0.16	0.65	1064	1439	−0.98
CL137-11	443	0.282506	0.000017	0.001200	0.000015	0.047476	0.000910	−9.42	−0.02	0.60	1061	1426	−0.96
CL137-12	449	0.282523	0.000019	0.001309	0.000016	0.050131	0.000563	−8.81	0.69	0.66	1040	1385	−0.96
CL137-13	456	0.282534	0.000018	0.000775	0.000008	0.028251	0.000333	−8.41	1.40	0.65	1009	1346	−0.98
CL137-14	456	0.282485	0.000017	0.000664	0.000012	0.023191	0.000377	−10.14	−0.30	0.60	1074	1453	−0.98
CL137-15	458	0.282514	0.000017	0.000810	0.000009	0.031069	0.000467	−9.14	0.70	0.60	1039	1392	−0.98
CL137-16	450	0.282491	0.000018	0.001263	0.000012	0.047978	0.000641	−9.93	−0.39	0.64	1083	1455	−0.96
CL137-17	457	0.282506	0.000016	0.000704	0.000016	0.025225	0.000517	−9.39	0.45	0.55	1046	1407	−0.98
CL137-18	453	0.282551	0.000017	0.000717	0.000007	0.025833	0.000387	−7.81	1.96	0.60	984	1308	−0.98
CL137-19	459	0.282460	0.000019	0.000696	0.000008	0.025590	0.000266	−11.03	−1.15	0.67	1111	1509	−0.98
CL137-20	445	0.282509	0.000025	0.001155	0.000016	0.044083	0.000528	−9.29	0.17	0.89	1055	1416	−0.97
CL133-01	437	0.282501	0.000034	0.004894	0.000044	0.197607	0.001938	−9.58	−1.39	1.21	1184	1507	−0.85
CL133-02	432	0.282539	0.000021	0.002196	0.000033	0.091290	0.001124	−8.25	0.64	0.76	1042	1375	−0.93
CL133-03	440	0.282530	0.000018	0.001350	0.000042	0.056032	0.001474	−8.54	0.74	0.65	1030	1375	−0.96
CL133-04	435	0.282490	0.000020	0.002049	0.000022	0.082446	0.001120	−9.97	−0.99	0.70	1108	1481	−0.94
CL133-05	442	0.282559	0.000027	0.002764	0.000035	0.107907	0.001518	−7.55	1.38	0.95	1029	1336	−0.92
CL133-06	441	0.282498	0.000016	0.001629	0.000028	0.069380	0.001489	−9.69	−0.47	0.56	1085	1452	−0.95
CL133-07	438	0.282530	0.000020	0.002508	0.000056	0.106517	0.002118	−8.57	0.35	0.72	1064	1398	−0.92
CL133-08	430	0.282584	0.000024	0.003845	0.000019	0.166747	0.001091	−6.65	1.72	0.87	1023	1305	−0.88
CL133-09	435	0.282546	0.000023	0.003086	0.000078	0.120525	0.003050	−8.00	0.68	0.82	1058	1375	−0.91
CL133-10	446	0.282474	0.000018	0.001390	0.000025	0.052370	0.000835	−10.54	−1.15	0.64	1112	1499	−0.96
CL133-11	441	0.282434	0.000017	0.001116	0.000008	0.046094	0.000453	−11.95	−2.57	0.59	1159	1586	−0.97
CL133-12	431	0.282457	0.000021	0.002325	0.000027	0.080778	0.000570	−11.13	−2.32	0.74	1164	1561	−0.93
CL133-13	427	0.282529	0.000029	0.004930	0.000069	0.217394	0.003426	−8.58	−0.58	1.04	1141	1448	−0.85
CL102-01	417	0.282660	0.000015	0.001293	0.000004	0.050140	0.000080	−3.97	4.85	0.52	845	1096	−0.96
CL102-02	414	0.282705	0.000020	0.001903	0.000015	0.075942	0.000673	−2.36	6.24	0.72	794	1006	−0.94
CL102-03	424	0.282659	0.000017	0.001647	0.000007	0.063833	0.000446	−3.99	4.89	0.61	854	1100	−0.95
CL102-04	417	0.282699	0.000019	0.002111	0.000011	0.082923	0.000327	−2.58	6.03	0.66	807	1022	−0.94
CL102-05	413	0.282687	0.000025	0.001384	0.000010	0.053342	0.000657	−3.01	5.71	0.90	809	1039	−0.96
CL102-06	428	0.282721	0.000022	0.001484	0.000014	0.058897	0.000287	−1.81	7.19	0.79	762	956	−0.96
CL102-08	420	0.282658	0.000025	0.001686	0.000017	0.067279	0.000284	−4.04	4.73	0.87	857	1106	−0.95
CL102-09	429	0.282681	0.000024	0.001605	0.000007	0.062820	0.000161	−3.22	5.76	0.85	822	1047	−0.95
CL102-10	425	0.282626	0.000026	0.001674	0.000009	0.066634	0.000352	−5.18	3.70	0.93	903	1175	−0.95
CL102-11	416	0.282691	0.000025	0.001511	0.000006	0.060393	0.000241	−2.86	5.89	0.88	805	1029	−0.95
CL102-12	421	0.282683	0.000029	0.001568	0.000005	0.062157	0.000490	−3.14	5.69	1.04	818	1046	−0.95
CL102-14	418	0.282712	0.000026	0.001155	0.000005	0.045211	0.000459	−2.14	6.76	0.94	769	976	−0.97

(*Continued*)

https://doi.org/10.1017/S0016756820000126 Published online by Cambridge University Press

Table 2. (*Continued*)

Sample	Age (Ma)	$^{176}Hf/^{177}Hf$	2σ	$^{176}Lu/^{177}Hf$	2σ	$^{176}Yb/^{177}Hf$	2σ	$\epsilon_{Hf}(0)$	$\epsilon_{Hf}(T)$	2σ	TDM1	TDM2	fLu/Hf(s)
CL102-15	415	0.282636	0.000027	0.001352	0.000003	0.052443	0.000163	−4.82	3.95	0.94	881	1153	−0.96
CL102-17	423	0.282676	0.000025	0.001645	0.000005	0.065222	0.000539	−3.39	5.46	0.87	830	1062	−0.95
CL106-01	410	0.282670	0.000017	0.001440	0.000003	0.059647	0.000128	−3.59	5.04	0.59	833	1079	−0.96
CL106-02	411	0.282658	0.000015	0.001699	0.000006	0.070071	0.000423	−4.04	4.53	0.55	857	1112	−0.95
CL106-03	413	0.282672	0.000017	0.001032	0.000009	0.040361	0.000095	−3.54	5.28	0.60	822	1066	−0.97
CL106-04	409	0.282669	0.000017	0.001517	0.000009	0.062681	0.000510	−3.63	4.95	0.59	837	1083	−0.95
CL106-5	408	0.282687	0.000015	0.001335	0.000002	0.054582	0.000136	−3.01	5.62	0.53	808	1041	−0.96
CL106-6	410	0.282657	0.000015	0.001425	0.000003	0.058687	0.000150	−4.05	4.59	0.54	852	1108	−0.96
CL106-7	410	0.282688	0.000013	0.001540	0.000001	0.063666	0.000158	−2.98	5.62	0.46	811	1042	−0.95
CL106-8	413	0.282670	0.000014	0.001388	0.000002	0.057233	0.000158	−3.59	5.12	0.49	832	1076	−0.96
CL106-9	406	0.282675	0.000016	0.002109	0.000010	0.088685	0.000160	−3.41	4.96	0.56	841	1081	−0.94
CL106-10	414	0.282691	0.000017	0.001431	0.000003	0.058307	0.000239	−2.85	5.86	0.59	803	1029	−0.96
CL106-11	411	0.282683	0.000014	0.001451	0.000017	0.059761	0.000547	−3.16	5.48	0.49	816	1051	−0.96
CL106-12	410	0.282661	0.000013	0.001288	0.000008	0.053969	0.000148	−3.93	4.74	0.46	843	1098	−0.96
CL106-13	404	0.282653	0.000017	0.001583	0.000021	0.072938	0.001436	−4.20	4.28	0.61	861	1123	−0.95
CL106-14	413	0.282678	0.000014	0.001330	0.000001	0.055143	0.000234	−3.31	5.42	0.48	820	1057	−0.96
CL106-15	408	0.282703	0.000014	0.001414	0.000002	0.058972	0.000275	−2.45	6.14	0.49	787	1007	−0.96
CL106-16	413	0.282693	0.000014	0.001347	0.000003	0.055967	0.000300	−2.79	5.94	0.48	799	1024	−0.96
CL106-17	409	0.282654	0.000015	0.001028	0.000006	0.041569	0.000428	−4.19	4.54	0.53	848	1110	−0.97
CL106-18	409	0.282677	0.000016	0.001417	0.000006	0.057940	0.000377	−3.37	5.25	0.55	824	1065	−0.96
CL106-19	407	0.282659	0.000015	0.001261	0.000003	0.052164	0.000219	−4.01	4.60	0.52	846	1105	−0.96
CL106-20	408	0.282675	0.000012	0.001402	0.000002	0.057530	0.000194	−3.44	5.16	0.44	826	1070	−0.96

than the ideal are admitted into a thermally expanded lattice, but favoured elements are those closest to the ideal size.

The zircon grains of samples CL101 and CL108 are short column crystals (Fig. 3), with a length/width ratio in the range 1.5:1–3:1. The cathodoluminescence (CL) images show clear oscillatory zoning (Fig. 3). The Th/U ratios are in the ranges 0.76–1.91 (avg. 1.18) and 0.73–1.24 (avg. 0.98), respectively (Supplementary Table S1 in Supplementary Material available online at https://doi.org/10.1017/S0016756820000126), indicating that the zircons are of magmatic origin. Forty spots were analysed for each sample, and the $^{206}Pb/^{238}U$ mean ages are 510.7 ± 3.2 Ma and 501.3 ± 4.6 Ma, respectively (Fig. 4a, b), representing their crystallization ages.

Most of the zircon grains in samples CL128 and CL140 show prismatic features (Fig. 3), with a length/width ratio in the range 2:1–3:1, and the CL images show oscillatory zoning, with a few grains containing old inherited zircon cores. The Th/U ratios are in the ranges 0.13–1.71 (avg. 0.70) and 0.14–2.42 (avg. 1.02) (Supplementary Table S1 in Supplementary Material available online at https://doi.org/10.1017/S0016756820000126), respectively, showing features of magmatic origin. Forty points were analysed for each sample, and the $^{206}Pb/^{238}U$ mean ages are 483.7 ± 3.2 Ma and 493.9 ± 3.5 Ma (Fig. 4c, d), respectively, representing their crystallization ages.

The zircon grains of samples CL139 and CL143-5 are in the form of long columns (Fig. 3), with a length/width ratio ranging from 1.5:1 to 4:1, and show zonal textures in the CL images. The ratios of Th/U range from 0.17 to 1.58 (avg. 0.55) and 0.14 to 1.70 (avg. 0.68) (Supplementary Table S1 in Supplementary Material available online at https://doi.org/10.1017/S0016756820000126), respectively, revealing a magmatic origin for the zircons. The analysed 30 and 40 spots of samples CL139 and CL143-5 yielded $^{206}Pb/^{238}U$ mean ages of 469.7 ± 3.2 Ma and 478.9 ± 2.8 Ma, respectively (Fig. 5a, b), implying their crystallization ages.

The zircon grains of samples CL136 and CL137 are in long column crystal form, while a few are in short column form, with a length/width ratio ranging from 1.5:1 to 3.5:1, and show clear oscillatory zoning in the CL images (Fig. 3). The Th/U ratios range from 0.14 to 1.03 (avg. 0.32) and 0.26 to 1.03 (avg. 0.53), respectively (Supplementary Table S1 in Supplementary Material available online at https://doi.org/10.1017/S0016756820000126), reflecting a magmatic origin for the zircons. Thirty spots were analysed for each of the two samples, and the $^{206}Pb/^{238}U$ mean ages are 450.0 ± 3.5 Ma and 433.1 ± 6.1 Ma, respectively (Fig. 5c, d), representing their crystallization ages.

The zircon grains of samples CL102 and CL147 are prismatic, with a length/width ratio in the range 1:1–4:1, and show clear oscillatory zoning in the CL images (Fig. 3). The Th/U ratios range from 0.37 to 0.73 (avg. 0.53) and 0.31 to 0.60 (avg. 0.43), respectively (Supplementary Table S1 in Supplementary Material available online at https://doi.org/10.1017/S0016756820000126), showing

https://doi.org/10.1017/S0016756820000126 Published online by Cambridge University Press

Table 3. Geological features of the plutons from Mangya in this study

Sample No.	Name	Age (Ma)	Hf isotope	Texture	Mineral composition
CL101	quartz monzonite	510.7	−1.88 to −0.32	grey-white to grey-red in colour, medium grained (Fig. 2a)	Hbl (~15 %), Pl (40–45 %), Kfs (30–35 %), Qtz (~5 %), Zr, Ap (Fig. 2a2)
CL108	quartz monzonite	501.3	−3.51 to −0.35		
CL140	diorite	493.9	0.04 to 2.36	grey in colour, medium grained	Hbl (~30 %), Pl (~ 65 %)
CL128	diorite	483.7	1.24 to 3.90	grey in colour, medium-grained (Fig. 2b)	Hbl (~35 %), Pl (~ 60 %) (Fig. 2b2)
CL139	quartz monzodiorite	469.7	0.05 to 3.05	grey-black in colour, fine to medium grained (Fig. 2c)	Hbl (8–10 %), Pl (65–70 %), Kfs (10 %) Qtz (~ 5 %), Zr, Ap (Fig. 2c2)
CL143-5	granodiorite	478.9	0.41 to 2.34	offwhite in colour, medium grained (Fig. 2d)	Pl (60–65 %), Kfs (10 %) Qtz (~ 20 %), Zr, Ap (Fig. 2d2)
CL130	monzonitic granite	450.0		grey-black in colour, fine to medium grained (Fig. 2e)	Qtz (~ 25 %), Pl (~ 35 %), Kfs (~ 35 %), Zr, Ap (Fig. 2e2)
CL133	monzonitic granite		−2.75 to −0.47, 0.35 to 4.72		
CL136	monzonitic granite	433.1	−1.27 to −0.02, 0.31 to 1.96		
CL102	alkali feldspar granite	418.8	3.70 to 7.19	flesh pink colour, medium to coarse grain (Fig. 2f)	Qtz (~ 25 %), Kfs (~ 70 %), Bi (1–2 %), Zr, Ap (Fig. 2f2)
CL114	alkali feldspar granite		4.53 to 6.14		
CL147	alkali feldspar granite	409.0			

Ap – apatite; Bi – biotite; Hbl – hornblende; Kfs – K-feldspar; Pl – plagioclase; Qtz – quartz; Zr – zircon.

features of magmatic origin. For each sample, 31 and 30 points were analysed, and the $^{206}Pb/^{238}U$ mean ages are 418.8 ± 3.7 Ma and 409.0 ± 2.5 Ma (Fig. 5e, f), respectively, implying their crystallization ages.

Thus, the quartz monzonites were emplaced at *c.* 511–501 Ma; the diorites at *c.* 494–483 Ma; the quartz monzodiorites at *c.* 479–469 Ma; the monzonitic granites at *c.* 450–433 Ma; and the alkali feldspar granites at *c.* 419–409 Ma.

4.c Geochemistry

4.c.1 Major elements

In the Mangya plutons, the monzonitic granites and the alkali feldspar granites contain the highest content of SiO_2 and $(Na_2O + K_2O)$, and the lowest ratios of Na_2O/K_2O. The diorites have the lowest content of $(Na_2O + K_2O)$, with the highest ratios of Na_2O/K_2O (Table 1). The data of the quartz monzonites plotted in the alkaline area, while those of the other plutons plotted in the sub-alkaline area (Fig. 6a). The aluminium saturation index (ASI) of the plutons ranges from 0.77 to 0.91, 0.97 to 1.15, 1.11 to 1.19 and 0.96 to 1.00, respectively, indicating that the plutons for the quartz monzonites and alkali feldspar granites are aluminous, the diorites quartz monzodiorites and granodiorites are aluminous to weak peraluminous, and the monzonitic granites are peraluminous (Fig. 6b). Most of the data of the Mangya plutons plotted in the Magnesian area (Fig. 6c), except that for the plutons for the alkali feldspar granites, which fell in the Ferroan area (Fig. 6c). The data of all plutons are mostly in the MK CA to HK CA area, except that of the quartz monzonites, which plotted in the SHO area (Fig. 6d). The SiO_2 content of the diorites, granodiorites and the quartz monzodiorites displays an obvious negative correlation with P_2O_5 (Fig. 7a). All the plutons display negative correlation in the diagram of SiO_2 vs TiO_2, FeO^T and MgO (Fig. 7b, d, e).

4.c.2 Trace elements

All the samples analysed are depleted in high-field-strength elements (HFSEs) and are partially enriched in large-ion lithophile elements (LILEs), although the contents of the elements vary slightly in different samples. On a trace element spider diagram, the quartz monzonites display negative anomalies of Nb, Ta, Ti, P and Sr (Fig. 8a), and the diorites and the quartz monzodiorites show negative anomalies of Ba, Nb, Ta, P, and positive anomalies of Sr, Zr and Hf (Fig. 8c). The monzonitic granites show significantly negative Ti and P anomalies and weak negative Nb and Ta anomalies, while showing positive anomalies of Zr and Hf (Fig. 8e). The alkali feldspar granites show significant negative Ba, Sr, Ti and P anomalies (Fig. 8g).

4.c.3 Rare earth elements

The total content of the rare earth elements (TREEs) for the quartz monzonites is in the range 255.48–339.51 ppm, and the LREE/HREE ratio ranges from 10.13 to 12.43, exhibiting right-slanting curves with a weak negative Eu anomaly (Eu* = 0.74–0.93) (Table 1; Fig. 8b). The TREEs of the diorites and that of the quartz monzodiorites vary greatly (Fig. 8d). The TREEs of the diorites is 53.65 ppm, and the LREE/HREE ratio is 12.03, with a weak positive Eu anomaly (Eu* = 1.48) (Table 1). The TREEs of the other plutons ranges from 27.65—to 295.69 ppm (Table 1), and sample CL143-5 shows a strong positive Eu anomaly (Eu* = 5.82), while sample CL139 displays a weak negative Eu anomaly (Eu* = 0.73) (Fig. 8d). The TREEs of the monzonitic granites is in the range 31.14–190.69 ppm, with the LREE/HREE ratios ranging from 4.11 to 15.56 (Table 1). The TREEs of the alkali feldspar granites ranges from 197.63—to 506.99 ppm, with LREE/HREE ratio in the range 5.09–10.48, and the samples show strong negative Eu anomalies (Eu* = 0.14–0.24) (Table 1; Fig. 8h).

https://doi.org/10.1017/S0016756820000126 Published online by Cambridge University Press

4.c.4 Hf isotopes

Samples CL101 and CL108 were selected from the quartz monzonites for Hf isotopic analysis, and 10 and 32 zircon grains were analysed for each sample (Table 2). The $\epsilon_{Hf}(t)$ values are in the ranges −1.88 to −0.32 (avg. −1.11) and −3.51 to −0.35 (avg. −1.77), and the t_{DM2} ages range from 1601 to 1476 Ma (avg. 1546 Ma) and 1670 to 1490 Ma (avg. 1573 Ma). These two samples contain two and one positive $\epsilon_{Hf}(t)$ values, with the t_{DM2} ages ranging from 1466 Ma to 1400 Ma and 1464 Ma, respectively (Fig. 9a).

Samples CL140 and CL128 were selected from the diorites for Hf isotopic analysis, and 20 and 23 zircon grains were analysed for each sample (Table 2). The $\epsilon_{Hf}(t)$ values of sample CL140 range from 1.24 to 3.90 (avg. 2.63), and the t_{DM2} ages range from 1381 to 1214 Ma (avg. 1297 Ma) (Fig. 9a). The $\epsilon_{Hf}(t)$ values of sample CL128 are positive, ranging from 0.04 to 2.36 (avg. 0.76), with three negative values (−0.66 to −0.06), and the t_{DM2} ages range from 1453 to 1309 Ma (avg. 1,405 Ma) (Fig. 9b).

Samples CL139 and CL143-5 were selected from the quartz monzodiorites and granodiorites for Hf isotopic analysis. Twenty-one zircon grains were analysed for each sample (Table 2). The $\epsilon_{Hf}(t)$ values are in the ranges 0.05–3.05 (avg. 1.01) and 0.41 to 2.34 (avg. 1.67), and the t_{DM2} ages range from 1447 to 1316 Ma (avg. 1383 Ma) and 1422 to 1283 Ma (avg. 1347 Ma), respectively. Sample CL139 includes four negative values (−0.31 to −0.03), with the t_{DM2} ages in the range 1464–1447 Ma (avg. 1456 Ma) (Fig. 9b).

Samples CL137 and CL133 were selected from the monzonitic granites for Hf isotopic analysis, and 20 and 13 zircon grains were analysed for each sample (Table 2). Both samples contain almost half negative $\epsilon_{Hf}(t)$ values ranging from −1.27 to −0.02 (avg. −0.53) and −2.57 to −0.47 (avg. −1.01), with the t_{DM2} ages in the ranges 1,509–1453 Ma (avg. 1464 Ma) and 1586–1448 Ma (avg. 1,505 Ma), respectively. The remaining half positive $\epsilon_{Hf}(t)$ values of both samples range from 0.31 to 1.96 (avg. 0.78) and 0.35 to 1.72 (avg. 0.92), and the t_{DM2} ages are in the ranges 1416–1308 Ma (avg. 1,383 Ma) and 1,398–1,305 Ma (avg. 1,361 Ma) (Fig. 9c), respectively.

Samples CL102 and CL106 were selected from the alkali feldspar granites for Hf isotopic analysis, and 17 and 20 zircon grains were analysed for each sample, respectively. The $\epsilon_{Hf}(t)$ values of both samples are positive, ranging from 3.70 to 7.19 (avg. 5.49) and 4.53 to 6.14 (avg. 5.16), and the t_{DM2} ages are in the range 1175–976 Ma (avg. 1058 Ma) and 1112–1007 Ma (avg. 1071 Ma), respectively (Table 2; Fig. 9d).

5. Discussion

5.a Petrogenesis of the Mangya plutons

The quartz monzonites are proposed to be I-type granitic rocks according to mineral associations and geochemical features, i.e. negative correlation between SiO_2 and P_2O_5 (Fig. 7a) and rich in hornblende (Fig. 2a2), and all the samples plotted in I-type area (Fig. 10a, b) (Altherr *et al.* 2000). Zircon $\epsilon_{Hf}(t)$ values are mainly negative, with a few positive values (Fig. 9a), indicating that the source rocks are mainly composed of Mesoproterozoic (1,601–1,476 Ma) ancient crustal materials, mixed with a small amount of juvenile crustal components. Thus, we infer that the plutons were generated by the partial melting of the Mesoproterozoic crust triggered by the upwelling of basaltic magma during the spreading of the SAO.

The diorites show features of I-type plutons, i.e. rich in hornblende (Fig. 2b2), ASI < 1.00 (Fig. 6b), and Na_2O content is higher than K_2O content. As shown in Figure 10a, b, sample CL128 plotted in the I-type area. The diorite also shows features of oceanic adakite, i.e. enriched LILEs (Rb, Sr), depleted in HFSEs (Ba, Nb, Ta, P) (Fig. 8a), high content of Sr (605.18 ppm), low content of Y (6.89 ppm) and Yb (0.66 ppm), and high Sr/Y ratio (88) (Table 1). As shown in Figure 10c, d, the sample plotted in the adakite area, and in Figure 11a the samples plotted in the meta-basalt area. The geochemical characteristics of the sample are similar to the adakitic rocks generated by partial melting of subducted oceanic crust ($K_2O/Na_2O < 0.71$ and $CaO/Al_2O_3 > 0.2$) (Defant & Drummond, 1990), i.e. low ratios of K_2O/Na_2O (0.53) and CaO/Al_2O_3 (0.39) (Table 1), and positive $\epsilon_{Hf}(t)$ values (Fig. 9b). Hence we propose that subduction of the SAO occurred in this period, and these rocks were generated by the partial melting of the subducted slab.

The quartz monzodiorites and granodiorites show features of I-type plutons, i.e. negative correlation between SiO_2 and P_2O_5 (Fig. 7a), enriched in LILEs (Rb, Sr and K) and depleted in HFSEs (Nb, Ta and P) (Fig. 8c), and all samples plotted in the I-type area (Fig.10a, b). The rocks also contain high contents of Sr (427.93–565.66 ppm), low contents of Y (2.42–19.05 ppm) and Yb (0.37–1.43 ppm), with high ratios of Sr/Y (39.82–233.51), showing features of adakite. In Figure 11a, the samples plotted in the meta-greywacke area, and considering the positive $\epsilon_{Hf}(t)$ values (Fig. 9b), we propose that the rocks were generated by the partial melting of Mesoproterozoic–Neoproterozoic juvenile crust (1447–1283 Ma) triggered by the upwelling of the basaltic magma.

The monzonites show features of S-type granites, i.e. 1.24 > ASI > 1.44 (Fig. 6b), low content of TiO_2 (0.10–0.25 %), FeO^T (0.60–1.37%), CaO (0.40–1.61%) and MgO (0.34–0.49%), and $Na_2O\% < K_2O\%$ (Table 1) (Whalen *et al.* 1987; Ghani *et al.* 2013). The rocks also show features of I-type granites, i.e. negative correlation between P_2O_5 and SiO_2 (Fig. 7a), lack of Al-rich minerals, rich in LILEs (Rb and K) and depleted in HFSEs (Ta, P, Nb and Ti) (Fig. 8e, f). Therefore, we infer that these rocks might belong to the I–S transitional type. Considering the half positive and half negative $\epsilon_{Hf}(t)$ values of the samples, we suggest that the granites were generated by the partial melting of Mesoproterozoic juvenile crust (1398–1305 Ma) and Mesoproterozoic ancient crust (1586 Ma–1448 Ma) (Fig. 9c) triggered by the underplating of the basaltic magma from the deep-seated magma chambers.

The alkali-feldspar granites exhibit features of A-type granites, i.e. 1.00 > ASI > 0.96 (Fig. 7b), enriched in SiO_2 (76.81–78.53%) and $(Na_2O + K_2O)$ (7.91–8.89%), lack of CaO (0.34–0.54%) and MgO (0.11–0.14%) (Table 1), similar ratios of $10^4 \times Ga/Al$ (avg. 2.62) (Whalen *et al.* 1987; Ghani *et al.* 2013), and in Figure 10a, b, all the samples plotted in the A-type area. The $\epsilon_{Hf}(t)$ values are positive, indicating that the source rocks were composed of Neoproterozoic (1175–976 Ma) juvenile crustal materials. We propose that the granites were generated by the partial melting of the Neoproterozoic juvenile crust triggered by substantial emplacement of mafic magma.

https://doi.org/10.1017/S0016756820000126 Published online by Cambridge University Press

Fig. 2. (Colour online) (a, c–f) Field pictures showing the characteristics of the outcrops. (b) Hand specimen showing the texture of the diorite. (a2–f2) Photomicrographs of the samples showing the mineral associations. Bt – biotite; Hbl – hornblende; Kfs – K-feldspar; Pl – plagioclase. Q – quartz.

5.b Episodes of magmatic events in the AMOB

The Mangya plutons preserve abundant information for the Palaeozoic tectonic evolution in the SAOB. Based on our new data for the Mangya plutons and previous studies, we divide the early Palaeozoic granitic magmatism in the AMOB into six episodes.

Episode 1 (510.7–493.9 Ma);
Episode 2 (483.7–458.3 Ma);
Episode 3 (450.0–433.1 Ma);
Episode 4 (418.8–403.9 Ma);
Episode 5 (352–338 Ma) (Wu *et al.* 2018);
Episode 6 (265–264 Ma) (Wu *et al.* 2014, 2018).

5.c Geodynamic processes

Zhang *et al.* (2010) and Liu *et al.* (2013, 2015) proposed northward subduction of the oceanic crust of the SAO (Zheng 2012; Zheng *et al.* 2013), which closed at 500 Ma. The HP and UHP metamorphic belts

https://doi.org/10.1017/S0016756820000126 Published online by Cambridge University Press

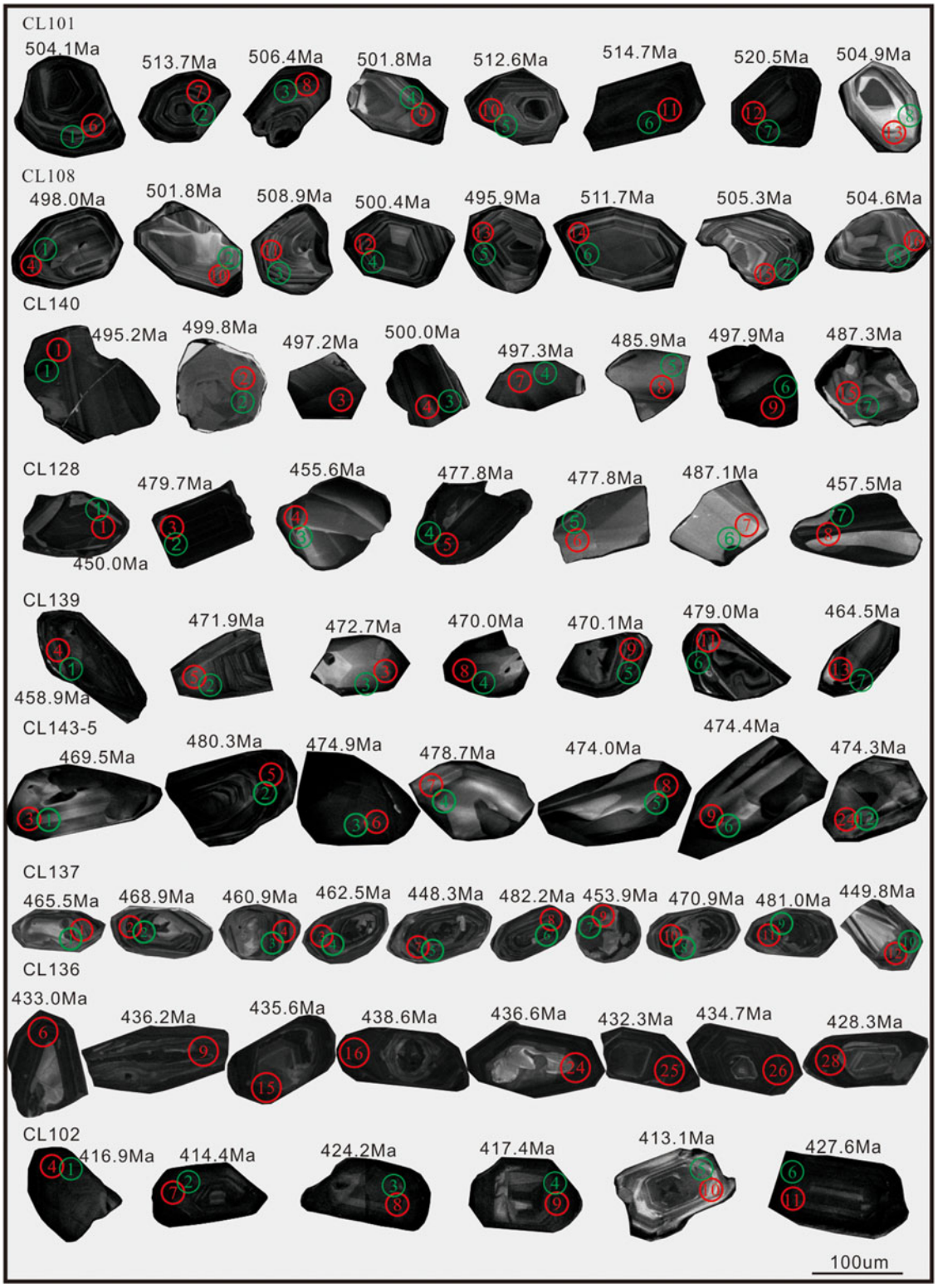

Fig. 3. (Colour online) CL images and U–Pb ages of the plutons in the Mangya area. Red circles – analysed spots of LA-ICP-MS analysis; green circles – analysed spots of Lu–Hf analysis.

in the SAOB were formed during the northward subduction of the SAO, and were uplifted twice at 450 Ma and 420 Ma (Liu *et al.* 2013), respectively. However, according to the previous studies and new data for the Mangya plutons, we suggest that the subduction of the SAO probably occurred after 483.7 Ma, as discussed below.

Zircon Lu–Hf isotopic analyses show that the $\epsilon_{Hf}(t)$ values of the Mangya plutons all straddled the chondritic unifractionated reservoir (CHUR) line (Fig. 9). Therefore, we propose subduction of the oceanic crust of the SAO in the Early Palaeozoic. For the plutons, the Th/Ta ratios range from 7.17 to 13.60 (avg. 10.94),

https://doi.org/10.1017/S0016756820000126 Published online by Cambridge University Press

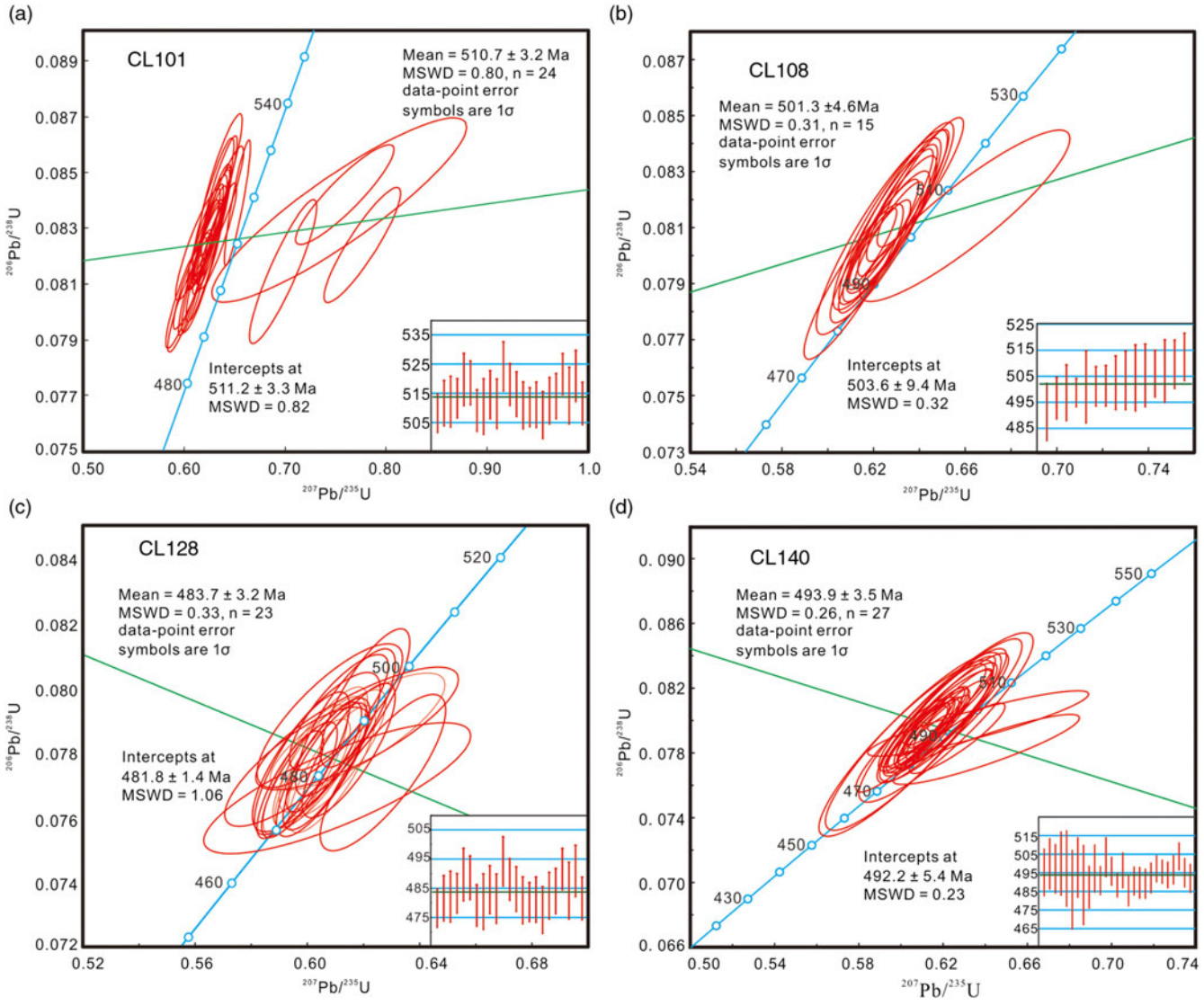

Fig. 4. (Colour online) U–Pb concordia diagram for the zircon grains of the plutons in the Mangya area.

16.12 to 510.01 (avg. 183.57), 7.84 to 33.35 (avg. 18.31) and 4.57 to 11.02 (avg. 8.15), respectively (Table 1). The ratios for the diorites, quartz monzodiorites and granodiorites vary greatly, and are closer to ocean island arc (OIA) rocks, while the quartz monzonites and the monzonitic granites are closer to active continental margin (ACM) rocks, and the alkali feldspar granites are closer to the OIA rocks (Foley, 1990; Sajona *et al.* 1996; Gorton & Schandl, 2000). As shown in Fig. 11c, d, and according to the geochemical and Hf isotopic data, we infer that the quartz monzonites were formed in an extending and thinning environment during the spreading of the SAO (Wu *et al.* 2014, 2016, 2018), the diorites, quartz monzodiorites and granodiorites are related to the subduction of the oceanic crust of the SAO, the monzonitic granites were generated in a syn-collision setting, indicating the closure of the SAO and the collision of the QB with the SACB, and the alkali feldspar granites were generated in post-orogenic extensional environment.

Thus, we propose a model for the early Palaeozoic tectonic evolution in the SAOB based on our new data and previous studies. From 511 to 494 Ma, a series of magmatic events occurred during the spreading of the SAO, and episode one plutons formed, showing I-type granitic features (Fig. 12a). The SAO began sinking from 484 Ma to 458 Ma, and large-scale I-type plutons formed at the northern margin of the AMOB (Fig. 12b). At the early stage in this period, a series of adakitic rocks were generated by the partial melting of the subducted slab of the SAO. Subsequently, the upwelling of the deep-seated magma caused partial melting of the lower crust and large scale I-type plutons were generated. The deep subduction of the continental crust occurred in this period, and the subducted continental crust underwent UHP metamorphism (Fig. 12b). From 450 Ma to 433 Ma, the SAO closed, the QB collided with the SACB resulting from the dragging of the previous sinking oceanic crust and break-off of the subducted SAO oceanic slab occurred (Fig. 12c). As the magmatic events continued, isostatic adjustment and extension occurred among different blocks which formed during the orogeny in the SAOB, resulting in the formation of deep-seated magma chambers. The heat provided by the mafic magma triggered the partial melting of the upper crust, and a series

https://doi.org/10.1017/S0016756820000126 Published online by Cambridge University Press

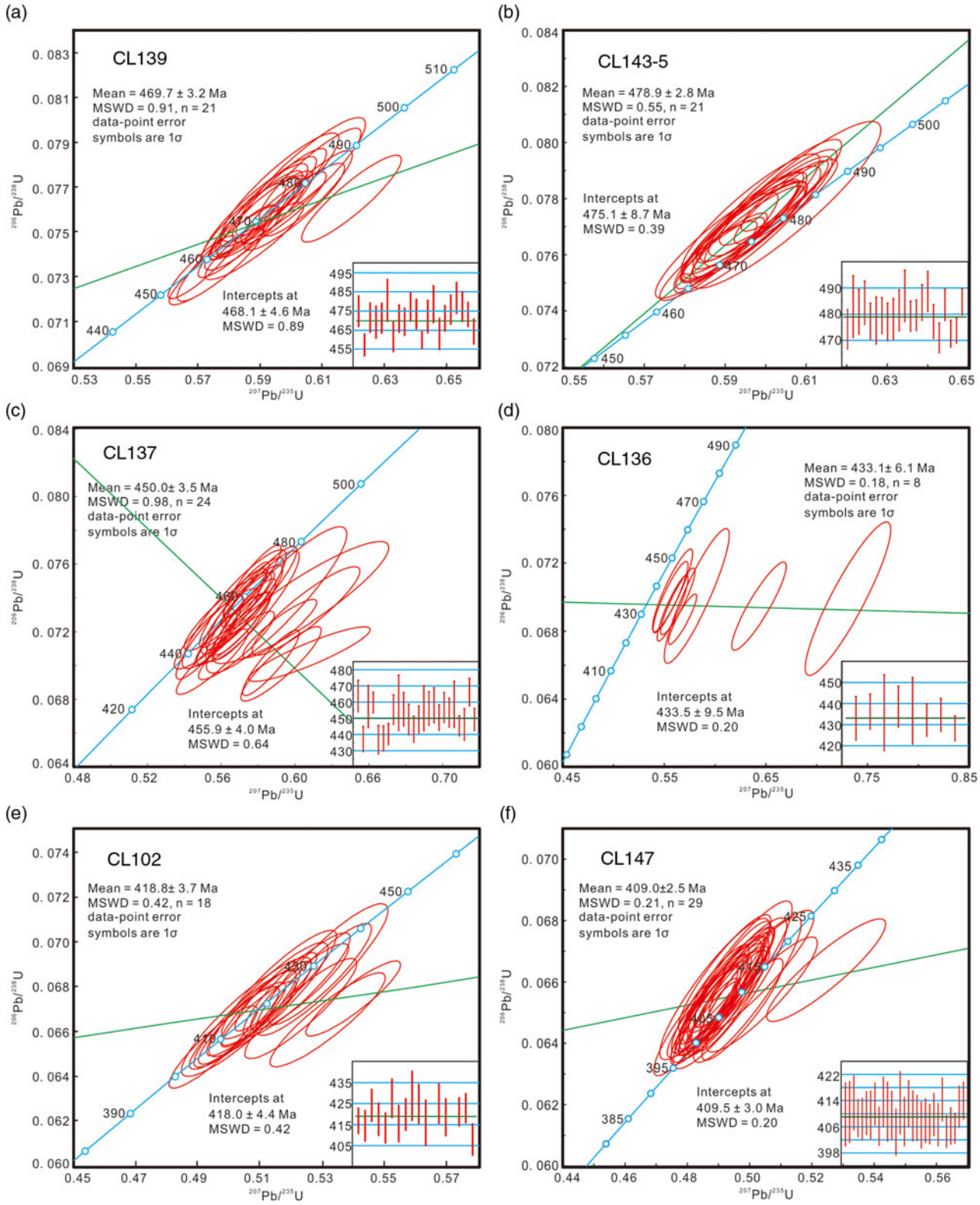

Fig. 5. (Colour online) U–Pb concordia diagram for the zircon grains of the plutons in the Mangya area.

https://doi.org/10.1017/S0016756820000126 Published online by Cambridge University Press

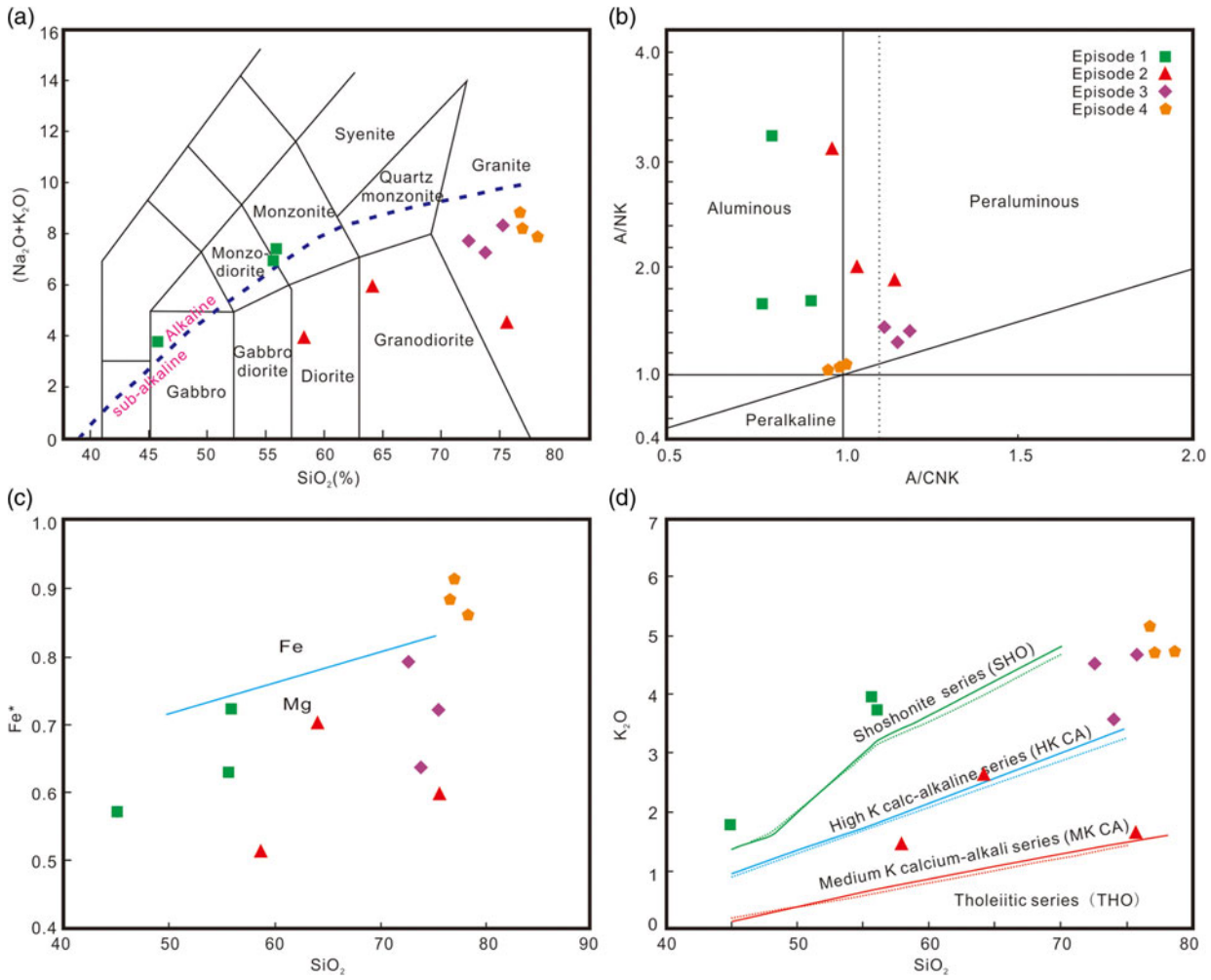

Fig. 6. (Colour online) (a) SiO_2–($Na_2O + K_2O$) diagram for the plutons in the Mangya area (after Middlemost, 1994; Irvine & Baragar, 1971). (b) A/CNK–A/NK diagram (Rickwood, 1989); (c) SiO_2–Fe* diagram (Frost & Frost, 2008); (d) K_2O–SiO_2 diagram (Maniar & Piccoli, 1989). Fe* = $FeO^T/(FeO^T + MgO)$.

of I–S transitional type granites formed (Fig. 12c). From 419 Ma to 404Ma, the AMOB was in a post-orogenic extensional environment triggered by the delamination of the sinking oceanic crust, and A-type granites were extensively generated (Fig. 12d). From 352 to 338 Ma, a series of S-type granites were generated triggered by the subduction of the Palaeo Tethys and the Palaeo Asian oceans, and the crust of the Altyn and Qilian orogenic belt thickened (Wu *et al.* 2018). From 265 to 264 Ma, some I-type granites were generated, resulting from the reactivation of the ASSF (Wu *et al.* 2018).

6. Conclusion

(1) According to our new data and previous studies, we divide the Early Palaeozoic plutons in the research area into four episodes: 511–494 Ma, 484–458 Ma, 450–433 Ma and 419404 Ma.

(2) Petrochemical and zircon Hf isotopic studies show that: the quartz monzonites were generated by partial melting of Mesoproterozoic ancient crust; the diorites were generated by partial melting of the continental lithospheric mantle; the quartz monzodiorites and granodiorites were generated by partial melting of Mesoproterozoic–Neoproterozoic juvenile crust; the monzonitic granites were generated by partial melting of Mesoproterozoic juvenile and ancient crusts; the alkali feldspar granites were derived from Neoproterozoic juvenile crust.

(3) We propose a model for the early Palaeozoic tectonic evolution in the SAOB. From 511 to 494 Ma, a series of magmatic events occurred during the spreading of the SAO, forming some I-type granitic rocks. The SAO began sinking from 484 to 458 Ma, forming large-scale I-type plutons at the northern margin of the AMOB. During 450–433 Ma, the SAO closed, and the QB collided with the SACB resulting from the dragging of the previous sinking oceanic crust. Break-off of the subducted SAO oceanic slab also occurred in this period. As the magmatic events continued, a series of I–S transitional type granites formed. During 419–404 Ma, the AMOB was in a post-orogenic extensional environment, and A-type granites were extensively generated.

https://doi.org/10.1017/S0016756820000126 Published online by Cambridge University Press

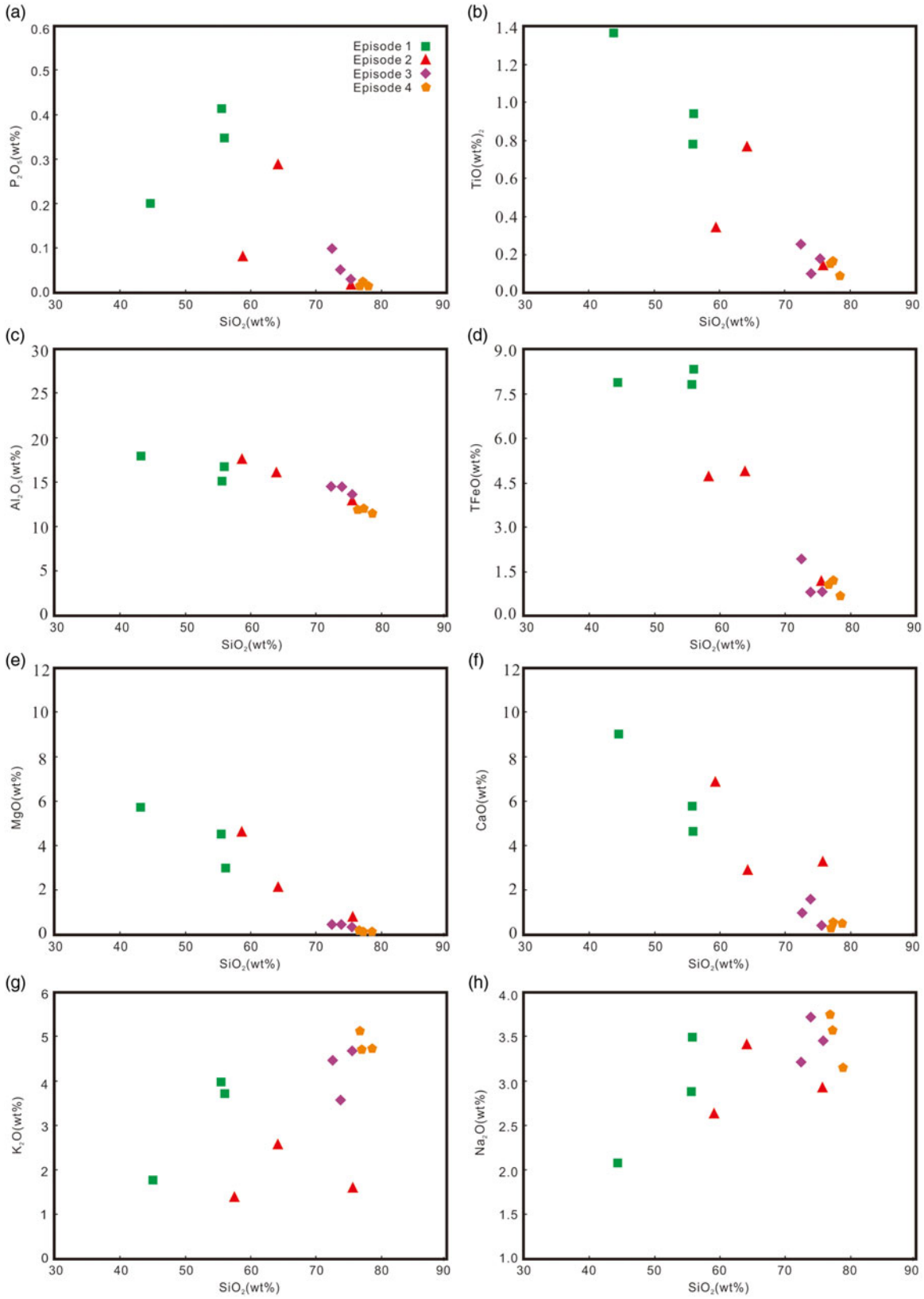

Fig. 7. (Colour online) Harker diagrams.

https://doi.org/10.1017/S0016756820000126 Published online by Cambridge University Press

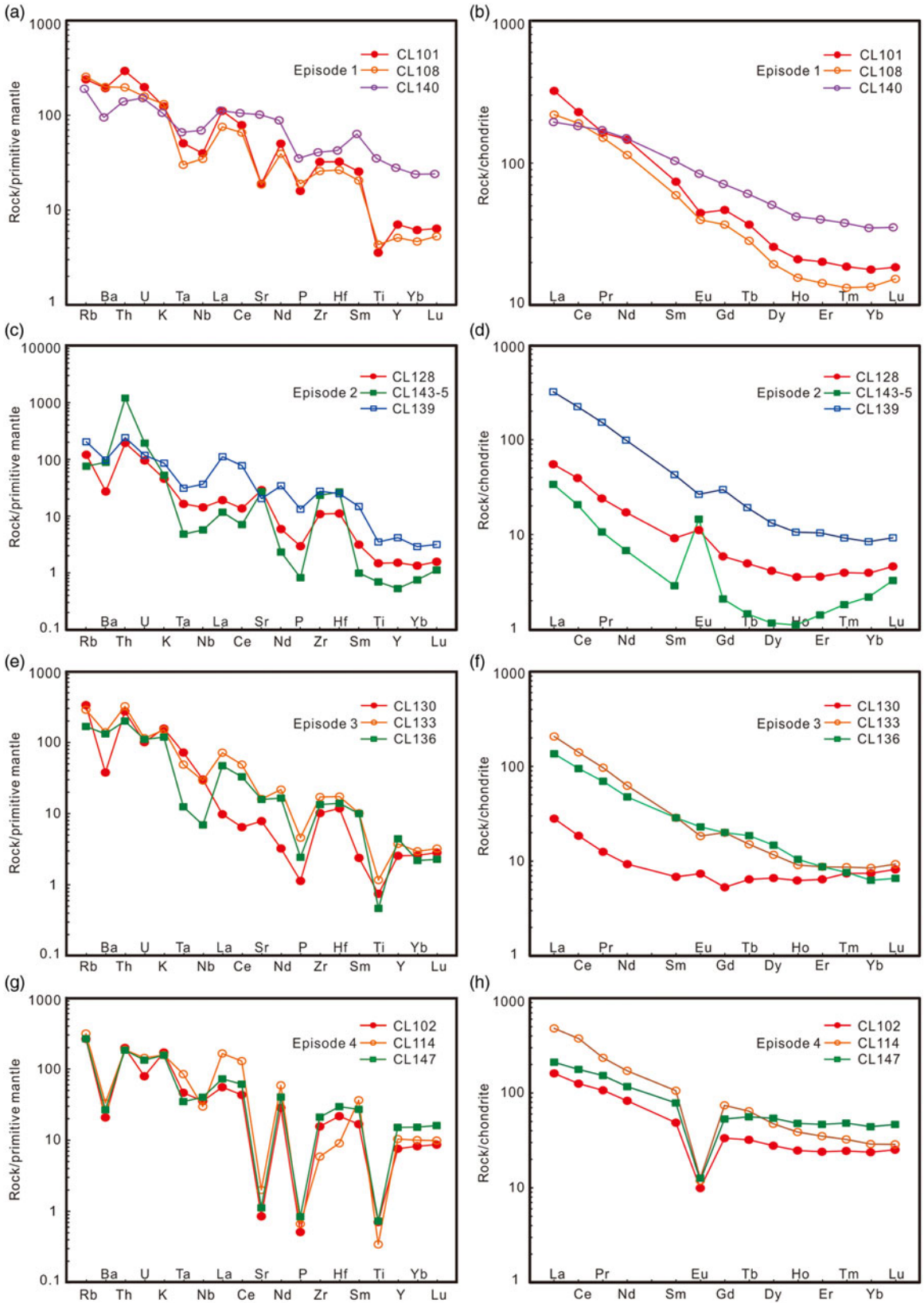

Fig. 8. (Colour online) Primitive-mantle-normalized trace-element spider diagrams (a, c, e, g) (normalizing values from Sun & McDonough, 1989) and chondrite–normalized REE distribution patterns (b, d, f, h) (normalizing values from Taylor & McLennan, 1985) of the plutons in the Mangya area.

https://doi.org/10.1017/S0016756820000126 Published online by Cambridge University Press

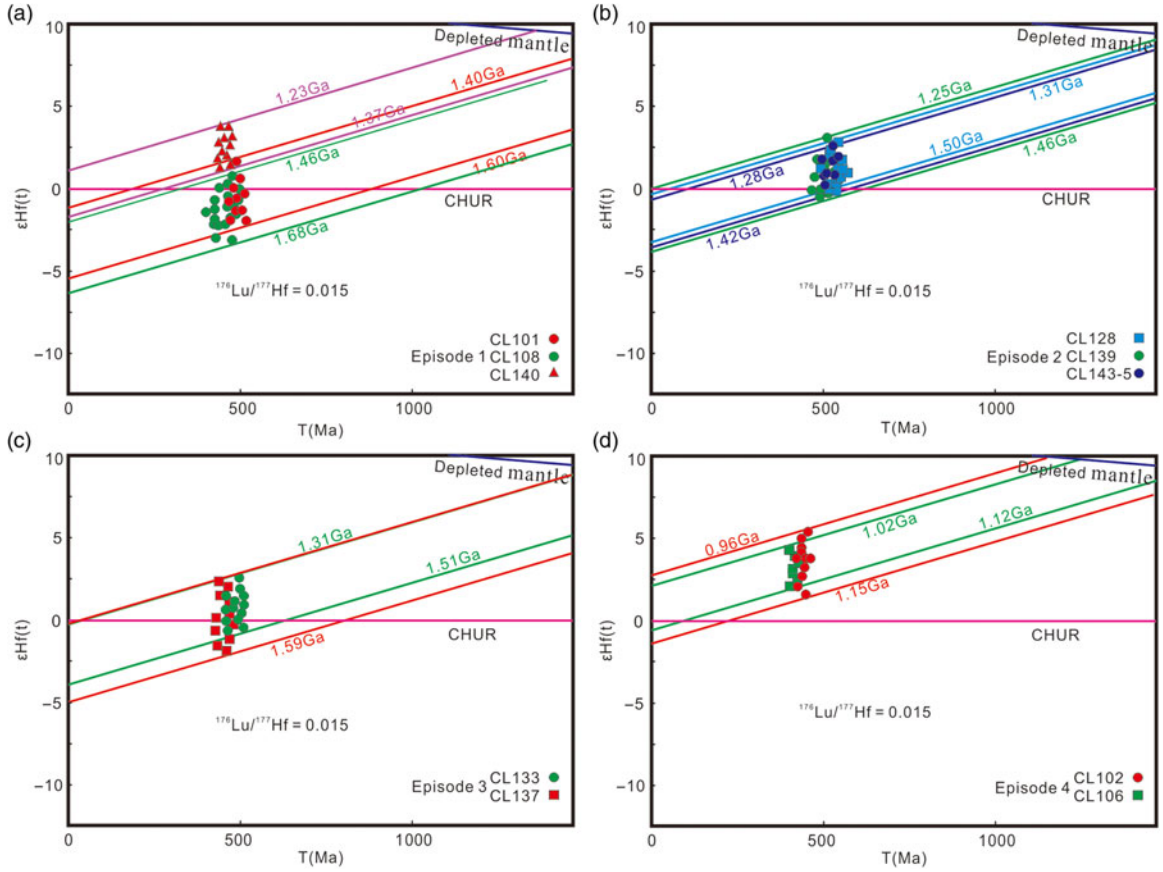

Fig. 9. (Colour online) Zircon $\epsilon_{Hf}(t)$ values vs age (Ma) for the plutons in the Mangya area.

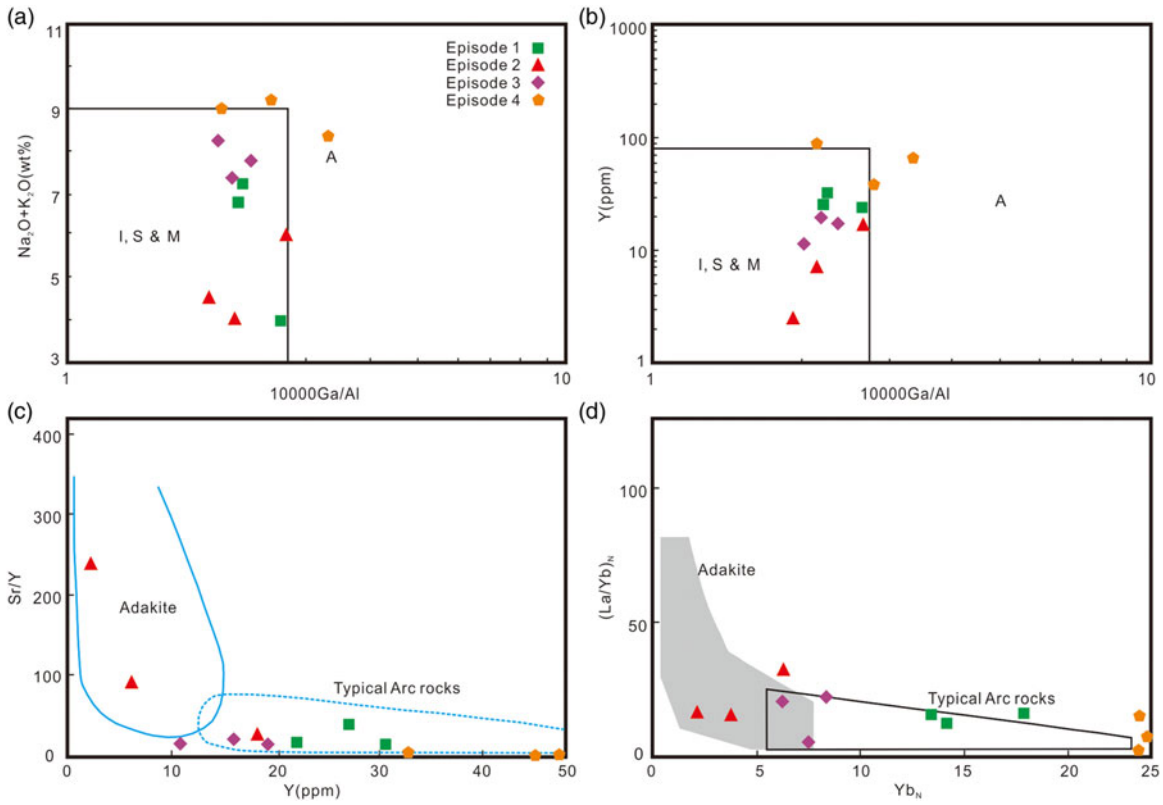

Fig. 10. (Colour online) (a, b) Plots of granite genetic types (after Whalen *et al.* 1987). (c) Plot of Sr/Y vs Y (after Drummond & Defant, 1990). (d) Plot of $(La/Yb)_N$–Yb_N (Defant & Drummond, 1990).

https://doi.org/10.1017/S0016756820000126 Published online by Cambridge University Press

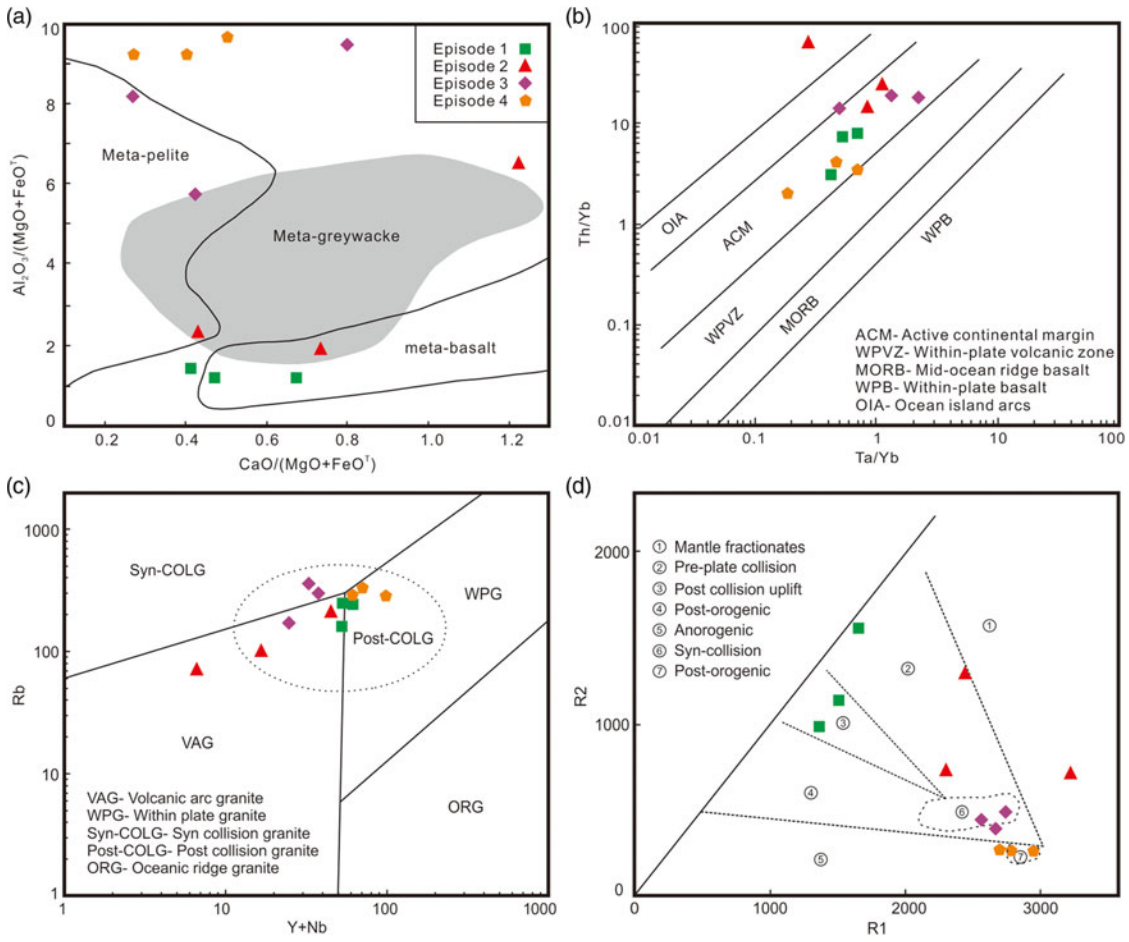

Fig. 11. (Colour online) (a) Plot of $Al_2O_3/(MgO + FeO^T)$ vs $CaO/(MgO + FeO^T)$ (Altherr *et al.* 2000). (b) Plot of Ta/Yb vs Th/Yb (Gorton & Schandl, 2000). (c) Plot of Rb vs (Y + Nb) (Pearce *et al.* 1984). (d) Plot of R1 vs R2 (Batchelor & Bowden, 1985). R1 = 4 * Si − 11 * (Na + K) − 2 * (Fe + Ti); R2 = 6 * Ca + 2 * Mg + Al; Si, Na, K, Fe, Ti, Ca, Mg and Al represent their atomic percentage contents.

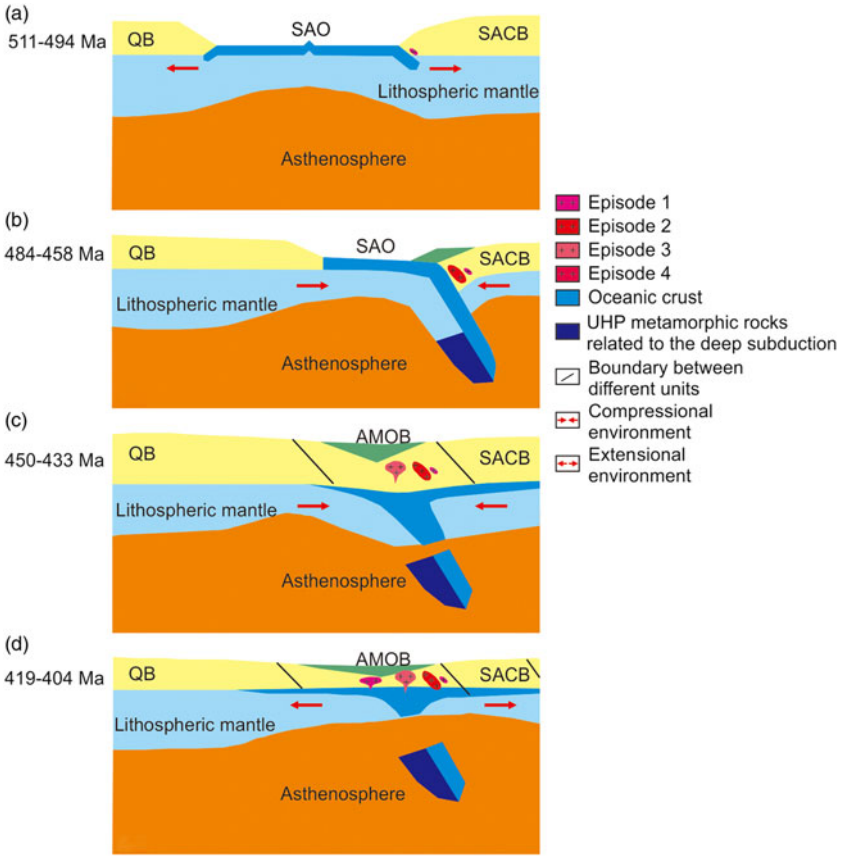

Fig. 12 (Colour online) Schematic model of the plate tectonic evolution and magmatism in the AMOB, looking west at the time of granites emplacement.

https://doi.org/10.1017/S0016756820000126 Published online by Cambridge University Press

Supplementary material. To view supplementary material for this article, please visit https://doi.org/10.1017/S0016756820000126

Acknowledgements. This work was supported by National Natural Science Foundation of China (Grant Nos. 41872071) and China Geological Survey Projects (grant Nos. DD20190006).

References

Altherr R, Holl A, Hegner E, Larger C and Kreuzer H (2000) High potassium, calc-alkaline I-type plutonism in the European Variscides: northern Vosges (France) and northern Schwarzwald (Germany). *Lithos* **50**, 51–73.

Batchelor RA and Bowden P (1985) Petrogenetic interpretation of granitoid rock series using multicationic parameters. *Chemical Geology* **48**, 43–55.

Bonin B (2004) Do coeval mafic and felsic magmas in post-collisional to within-plate regimes necessarily imply two contrasting, mantle and crustal, sources? A review. *Lithos* **78**, 1–24.

Cao YT, Liu L, Wang C, Kang L, Yang WQ, Liang S, Liao XY and Wang YW (2013) Determination and implication of the HP pelitic granulite from the Munabulake area in the South Altyn Tagh. *Acta Petrologica Sinica* **29**, 1727–39. (in Chinese with English abstract).

Castillo PR (2006) An overview of adakite petrogenesis. *Chinese Science Bulletin* **51**, 257–68.

Chu NC, Taylor RN, Chavagnac V, Nesbitt RW, Boella RM, Milton JA, German CR, Bayon G and Burton K (2002) Hf isotope ratio analysis using multicollector inductively coupled plasma mass spectrometry: an evaluation of isobaric interference corrections. *Journal of Analytical Atomic Spectrometry* **17**, 1567–74.

Defant MJ and Drummond MS (1990) Derivation of some modern arc magmas by melting of young subducted lithosphere. *Nature* **347**, 662–5.

Drummond MS and Defant MJ (1990) A model for trondhjemite–tonalite–dacite genesis and crustal growth via slab melting: Archean to modern comparisons. *Journal of Geophysical Research* **95**, 21503–21.

Foley SF (1990) Parallels in the origin of the geochemical signatures of island arc volcanics and continental potassic igneous rocks: the role of residual titanites. *Chemical Geology* **85**, 1–18.

Frost BR and Frost CD (2008) A geochemical classification for feldspathic igneous rocks. *Journal of Petrology* **49**, 1955–69.

Ghani AA, Searle M, Robb L and Chung SL (2013) Transitional I- and S-type characteristic in the Main Range Granite, Peninsular Malaysia. *Journal of Asian Earth Sciences* **76**, 225–40.

Gorton MP and Schandl ES (2000) From continents to island arcs: a geochemical index of tectonics setting for arc-related and within-plate felsic to intermediate volcanic rocks. *The Canadian Mineralogist* **38**, 1065–73.

Griffin WL, Wang X, Jackson SE, Pearson NJ, O'Reilly SR, Xu XS and Zhou XM (2002) Zircon chemistry and magma mixing, SE China: in-situ analysis of Hf isotopes, Tonglu and Pingtan igneous complexes. *Lithos* **61**, 237–69.

Guo ZP, Li WY, Zhang ZW, Gao YB, Zhang JW, Li K, Kong HL and Qian B (2015) Petrogenesis of Lumanshan granites in Hualong area of southern Qilian Mountain. Constraints from geochemistry, zircon U–Pb geochronology and Hf isotope. *Geology in China* **42**, 864–80 (in Chinese with English abstract).

Han FB, Chen BL and Cui LL (2012) Zircon SHRIMP U–Pb age of intermediate-acid intrusive rocks in Kaladawan area, eastern Altun Mountains, NW China, and its implications. *Acta Petrologica Sinica* **28**, 2277–91 (in Chinese with English abstract).

Hou KJ, Li YH, Zou TR, Qu XM, Shi YR and Xie GQ (2007) Laser ablation–MC–ICP–MS technique for Hf isotope microanalysis of zircon and its geological applications. *Acta Petrologica Sinica* **23**, 2595–604. (in Chinese with English abstract).

Irvine TN and Baragar WRA (1971) A guide to the chemical classification of the common volcanic rocks. *Canadian Journal of Earth Sciences* **8**, 523–48.

Jackson SE, Pearson NJ, Griffin WL and Belousova EA (2004) The application of laser ablation-inductively coupled plasma–mass spectrometry to in situ U–Pb zircon geochronology. *Chemical Geology* **211**, 47–69.

Kang L, Liu L, Wang C, Cao YT, Yang WQ, Wang YW and Liao XY (2014) Geochemistry and zircon U–Pb dating of Changshagou adakite from the South Altyn UHPM terrane: evidence of the partial melting of the lower crust. *Acta Geologica Sinica* **88**, 1454–65. (in Chinese with English abstract).

Kang L, Xiao PX, Gao XF, Xi RG and Yang ZC (2016) Chronology, geochemistry and petrogenesis of monzonitic granite and quartz diorite in Mangai Area: its inspiration to early Paleozoic tectonic-magmatic evolution of the southern Altun Tagh. *Acta Petrologica Sinica* **32**, 1731–48 (in Chinese with English abstract).

Kirkland CL, Smithies RH, Taylor RJM, Evans N and McDonald B (2015). Zircon Th/U ratios in magmatic environs. *Lithos*, **212–215**, 397–414.

Li SG, He YS and Wang SJ (2013) Process and mechanism of mountainroot removal of the Dabie Orogen: constraints from geochronology and geochemistry of post-collisional igneous rocks. *Chinese Science Bulletin* **58**, 4411–17 (in Chinese with English abstract).

Liu CH, Wu CL and Gao YH (2016) Age, composition, and tectonic significance of Palaeozoic granites in the Altynorogenic belt, China. *International Geology Review* **58**, 131–54.

Liu CH, Wu CL, Gao YH, Lei M and Qin HP (2015) Age, composition, and tectonic significance of Palaeozoic granites in the Altyn orogenic belt, China. *International Geology Review* **58**, 131–54.

Liu H, Wang GC, Yang ZJ, Luo YJ, Cao R and Huang WX (2013) Geochronology and geochemistry of the Qiashikansayi basalt and its constraint on the closure progress of the North Altyn Ocean. *Acta Geologica Sinica* **87**, 38–54 (in Chinese with English abstract).

Liu L, Che ZC, Wang Y, Luo JH, Wang JQ and Gao ZJ (1998) The evidence of Sm-Nd isochron age for the Early Paleozoic ophiolite in Mangya area, Altun Mountains. *Chinese Science Bulletin* **43**, 880–3 (in Chinese with English abstract).

Liu L, Che ZC, Wang Y, Luo JH and Chen DL (1999) The metrological characters and geotectonic setting of high-pressure metamorphic rock belts in Altun Mountains. Acta Petrologica Sinica **15**, 57–64 (in Chinese with English abstract).

Liu L, Sun Y, Xiao PX, Che ZC, Luo JH, Chen DL, Wang Y, Zhang AD, Chen L and Wang YH (2002) Discovery of ultrahighpressure magnesite –bearing garnet lherzolite (>3.8 GPa) in the Altyn Tagh, Northwest China. *Chinese Science Bulletin* **47**, 881–6.

Liu L, Kang L, Cao YT and Yang WQ (2015) Early Paleozoic granitic magmatism related to the processes from subduction to collision in South Altyn, NW China. *Science China (Earth Sciences)* **58**, 1513–22 (in Chinese with English abstract).

Liu L, Wang C, Chen DL, Zhang AD and Liu JG (2009) Petrology and geochronology of HP–UHP rocks from the South Altyn Tagh, northwestern China. *Journal of Asian Earth Sciences* **35**, 232–44.

Liu L, Wang C, Cao YT, Chen D, Kang L, Yang WQ and Zhu XH (2012) Geochronology of multi-stage metamorphic events: constraints on episodic zircon growth from the UHP eclogite in the South Altyn, NW China. *Lithos* **136–139**, 10–26.

Liu L, Yang JX, Chen DL, Wang C, Zhang CL, Yang WQ and Cao YT (2010) Progress and controversy in the study of HP–UHP metamorphic terranes in the West and Middle Central China orogen. *Journal of Earth Science – China* **21**, 581–97.

Liu L, Zhang AD, Chen DL, Yang JX, Luo JH and Wang C (2007a) Implications based on LA–ICP–MS zircon U–Pb ages of eclogite and its country rock from Jianggalesayi Area, Altyn Tagh, China. *Earth Science Frontiers* **14**, 98–107.

Liu L, Zhang JF, Green Ii HW, Jin ZM and Bozhilov KN (2007b) Evidence of former stishovite in metamorphosed sediments, implying subduction to >350 km. *Earth and Planetary Science Letters 263*. 180–91.

Ludwig KR (2003) *User's manual for Isoplot 3.0: a geochronological toolkit for Microsoft Excel*. Berkeley, CA: Berkeley Geochronology Center.

Ma ZP, Li XM, Sun JM, Xu XY, Lei YX, Wang LS and Duan XX (2009) Discovery of layered mafic–ultramafic intrusion in Changshagou, Altyn Tagh, and its geological implication: a pilot study on its petrological and geochemical characteristics. *Acta Petrologica Sinica* **25**, 793–804 (in Chinese with English abstract).

Maniar PD and Piccoli PM (1989) Tectonic discrimination of granitoids. *GSA Bulletin* **101**, 635–43.

Middlemost EAK (1994) Naming materials in magma/igneous rock system. *Earth-Science Reviews* **37**, 215–24.

Nasdala L, Hofmeister W, Norberg N, Martinson JM, Corfu F, Dörr W, Kamo SL, Kennedy AK, Kronz A, Reiners PW, Frei D, Kosler J, Wan YS, Götze J, Häger T, Kröner A and Valley JW (2008) Zircon M257 – a homogeneous natural reference material for the ion microprobe U–Pb analysis of zircon. *Geostandards & Geoanalytical Research* **32**, 247–65.

Pearce JA, Harris NBW and Tinele AG (1984) Trace element discrimination diagrams for the tectonic interpretation of granitic rocks. *Journal of Pertology* **25**, 956–83.

Pitcher WS (1983) Granite type and tectonic environment. In *Mountain Building Processes* (ed. K Hsu), pp. 19–40. London: Academic Press.

Rickwood PC (1989) Boundary lines within petrologic diagrams which use oxides of major and minor elements. *Lithos* **22**, 247–63.

Rubatto D (2002). Zircon trace element geochemistry: partitioning with garnet and the link between U–Pb ages and metamorphism. *Chemical Geology* **184**, 123–38.

Sajona FG, Maury RC, Bellon H, Cotton J and Defant M (1996) High field strength elements of Pliocene–Pleistocene island–arc basalts, Zamboanga Peninsula, Western Mindanao (Philippines). *Journal of Petrology* **37**, 693–726.

Scherer E, Munker C and Mezger K (2001) Calibration of the Lutetium–Hafnium clock. *Science* **293**, 683–7.

Sláma J, Košler J, Daniel JC, Crowley JL, Gerdes A, Hanchar JM, Horstwood MSA, Morris GA, Nasdala L, Norberg N, Schaltegger U, Schoene B, Tubrett MN and Whitehouse MJ (2008) Plešovice zircon – a new natural reference material for U–Pb and Hf isotopic microanalysis. *Chemical Geology* **249**, 1–35.

Song S, Niu Y, Su L, Zhang C and Zhang L (2014) Continental orogenesis from ocean subduction, continent collision/subduction, to orogen collapse, and orogen recycling: the example of the North Qaidam UHPM belt, NW China. *Earth-Science Reviews* **129**, 59–84.

Sun SS and McDonough WF (1989) Chemical and isotopic systematics of oceanic basalts: implications for mantle composition and processes. In *Magmatism in the Ocean Basins* (eds AD Saunders and MJ Norry), pp. 313–45. Geological Society of London, Special Publication no. 42.

Taylor SR and McLennan S (1985) *The Continental Crust: Its Composition and Evolution*. Oxford: Blackwell, 312 pp.

Wang C, Liu L, Xiao PX, Cao YT, Yu HY, Meert JG and Liang WT (2014) Geochemical and geochronologic constraints for Paleozoic magmatism related to the orogenic collapse in the Qimantagh–South Altyn region. Northwestern China. *Lithos* **202–203**, 1–20.

Whalen JB, Currie KL and Chappell BW (1987) A-type granites: geochemical characteristics, discrimination and petrogenesis. *Contributions to Mineralogy and Petrology* **95**, 407–19.

Wu CL, Chen HJ, Wu D and Ernstc WG (2018) Paleozoic granitic magmatism and tectonic evolution of the South Altun block, NW China: constraints from zircon U–Pb dating and Lu–Hf isotope geochemistry. *Journal of Asian Earth Sciences* **160**, 168–99.

Wu CL, Gao YH, Lei M, Qin HP, Liu CH, Li MZ, Frost BR and Joseph LW (2014) Zircon SHRIMP U-Pb dating, Lu-Hf isotopic characteristics and petrogenesis of the Palaeozoic granites in Mangya area, southern Altun, NW China. *Acta Petrologica Sinica* **30**, 2297–323 (in Chinese with English abstract).

Wu CL, Lei M, Zhang X, Chen HJ, Wu D and Li XX (2016) Petrogenesis and zircon Lu-Hf isotopic characteristics of the granites from the southern Altun area, Northwest China. *Geology in China* **43**, 1853–83 (in Chinese with English abstract).

Xu ZQ, Yang JS, Zhang JX, Jiang M, Li HB and Cui JW (1999) A comparison between the tectonic units on the two sides of the Altun sinistral strike fault and the mechanism of lithospheric shearing. *Acta Geologica Sinica* **73**, 193–205 (in Chinese with English abstract).

Yang JS, Wu CL and Shi RD (2002) Sheeted dike swarm in Hongliugou, northwest of the Altun region: evidence for seafloor spreading. *Geological Bulletin of China* **21**, 69–74 (in Chinese with English abstract).

Yu SY, Li SZ, Zhang JX, Peng YB, Somerville I, Liu YJ, Wang ZY, Li ZF, Yao Y and Li Y (2019) Multistage anatexis during tectonic evolution from oceanic subduction to continental collision: a review of the North Qaidam UHP Belt, NW China. *Earth Science Reviews* **191**, 190–211.

Zhang JX, Meng FC and Yu SY (2010) Two contrasting HP/LT and UHP metamorphic belts constraint on early Paleozoic orogeny in Qilian–Altun orogeny. *Acta Petrologica Sinica* **26**, 1967–1992 (in Chinese with English abstract).

Zhang HF, Yu H, Zhou DW, Zhang J, Dong YP and Zhang GW (2015) The meta–gabbroic complex of Fushui in North Qinling orogen: a case of syn-subduction mafic magmatism. *Gondwana Research* **28**, 262–75.

Zhang JX, Yu SY and Mattinson CG (2017) Early Paleozoic polyphase metamorphism in northern Tibet, China. *Gondwana Research* **41**, 267–89.

Zhang RY, Zeng ZC and Zhu WP (2016) LA–ICP–MS zircon U–Pb dating, geochemical features and their geological implications of Paxialayidang plutons on the Southern margin of Altyn Tagh. *Geological Review* **62**, 1283–99 (in Chinese with English abstract).

Zhao ZF, Dai LQ and Zheng YF (2013) Postcollisional mafic igneous rocks record crust–mantle interaction during continental deep subduction. *Scientific Reports* **3**, 3413. doi: 10.1038/srep03413.

Zhao ZF, Zheng YF, Zhang J, Dai LQ, Li QL and Liu XM (2012) Synexhumation magmatism during continental collision: evidence from alkaline intrusives of Triassic age in the Sulu orogen. *Chemical Geology* **328**, 70–88.

Zheng YF (2012) Metamorphic chemical geodynamics in continental subduction zones. *Chemical Geology* **328**, 5–48.

Zheng YF, Xia QX, Chen RX and Gao XY (2011) Partial melting, fluid supercriticality and element mobility in ultrahigh-pressure metamorphic rocks during continental collision. *Earth-Science Reviews* **107**, 342–74.

Zheng YF, Xiao WJ and Zhao GC (2013) Introduction to tectonics of China. *Gondwana Research* **23**, 1189–1206.

https://doi.org/10.1017/S0016756820000126 Published online by Cambridge University Press